Fig. 4. Immunohistochemical analyses of Tim in the hippocampus. Images of Tim staining in the pyramidal neurons in CA3 region at E17 (A), P0 (B) and P30 (C). Sections were stained with anti-Tim preabsorbed with the Tim-antigen (a) or GST-p75NTR fragment (b). Boxed areas in (b) were magnified in (c). Counterstaining was performed with heamatoxylin. Bar, 50 μm (A and B); 10 μm (C).

Wetzlar, Germany). Sections were mounted on Superfrost slides (Matsunami Glass Inc., Osaka, Japan) and stored at −80 °C. Sections were then incubated in methanol containing 3% hydrogen peroxide for 30 min to block nonspecific endogenous peroxidase activity. To retrieve the antigen, sections were autoclaved at 121 °C for 20 min in 10 mM Tris–HCl buffer (pH 9.0) containing 137 mM NaCl. The sections were then blocked in Blocking One (Nacalai Tesque, Tokyo, Japan) for 30 min at room temperature, and reacted with anti-Tim at 1:100 dilution overnight at 4 °C. For preabsorption of the antibody, purified antibody was incubated with GST-Tim fragment (aa 981–1198) for 2 h on ice before reaction with anti-Tim. As a negative control, GST-fused p75 neurotrophin receptor (NTR) fragment (aa 274–472) was used instead of the Tim antigen. Immnohistochemistry was processed using Vectastain ABC kit PK-4001 (Vector laboratories, Peterborough, UK). Briefly, sections were incubated with biotinylated secondary antibody for 2 h at room temperature. ABC reagent was then added to induce avidin/biotinylated enzyme complexes formation. The staining was visualized by 3,3′-diaminobenzidine tetrahydrochloride (DAB) and hydrogen peroxide, and counterstained by heamatoxylin. Images were obtained using BZ-9000 microscope (Keyence, Osaka, Japan).

2.8. In situ hybridization

Antisense RNA probe labeled with digoxigenin (DIG; Roche, Basel, Switzerland) was synthesized with full length mouse Tim. After fixation as mentioned in Section 2.4, the brains were cut by a cryostat (Leica Microsystems, Wetzlar, Germany) into 20 μm-coronal sections. The cryosections were acetylated using 3 M acetic anhydride in 0.1 M triethanolamine (pH 8.0), incubated in the prehybridization solution (Life technologies Inc., Japan, Tokyo) at 60 °C for 1 h, and hybridized with the DIG-labeled antisense (1 μg/l) diluted in the prehybridization solution at 60 °C for 16 h. Sections were then blocked with 2% blocking reagent (Roche)/10% normal sheep serum (Chemicon, CA, USA) for 1 h. Subsequently, sections were incubated with alkaline phosphatase-conjugated anti-DIG (Roche) and hybridized probes were visualized with nitro blue tetrazolium and 5-bromo-4-chloro-3-indoylphosphate (Ajioka et al., 2006). The sense riboprobe was used as the negative control.

2.9. Immunofluorescence

Immunofluorescence analysis was done as described (Nagata et al., 2009). Briefly, cells grown on 13-mm coverslips were fixed in 3.7% formaldehyde in PBS for 15 min, then treated with 0.2% Triton-X 100 for 5 min. Rhodamine-phalloidin (Cytoskeleton Inc., Denver, CO) and 4′,6-diamidino-2-phenylindole (DAPI) were used for the F-actin and DNA staining, respectively. Alexa Fluor 488- and 568-labeled IgG (Life technologies Inc., Japan, Tokyo) were used as secondary antibodies. Images were obtained using FV-1000 confocal laser microscope (Olympus, Tokyo, Japan).

3. Results and discussion

3.1. Production and characterization of an antibody for Tim

After preparation and affinity-purification of anti-Tim, specificity of the antibody was confirmed with COS7 cell lysates expressing GFP-Tim (Fig. 1A, upper left panel). Preincubation of the
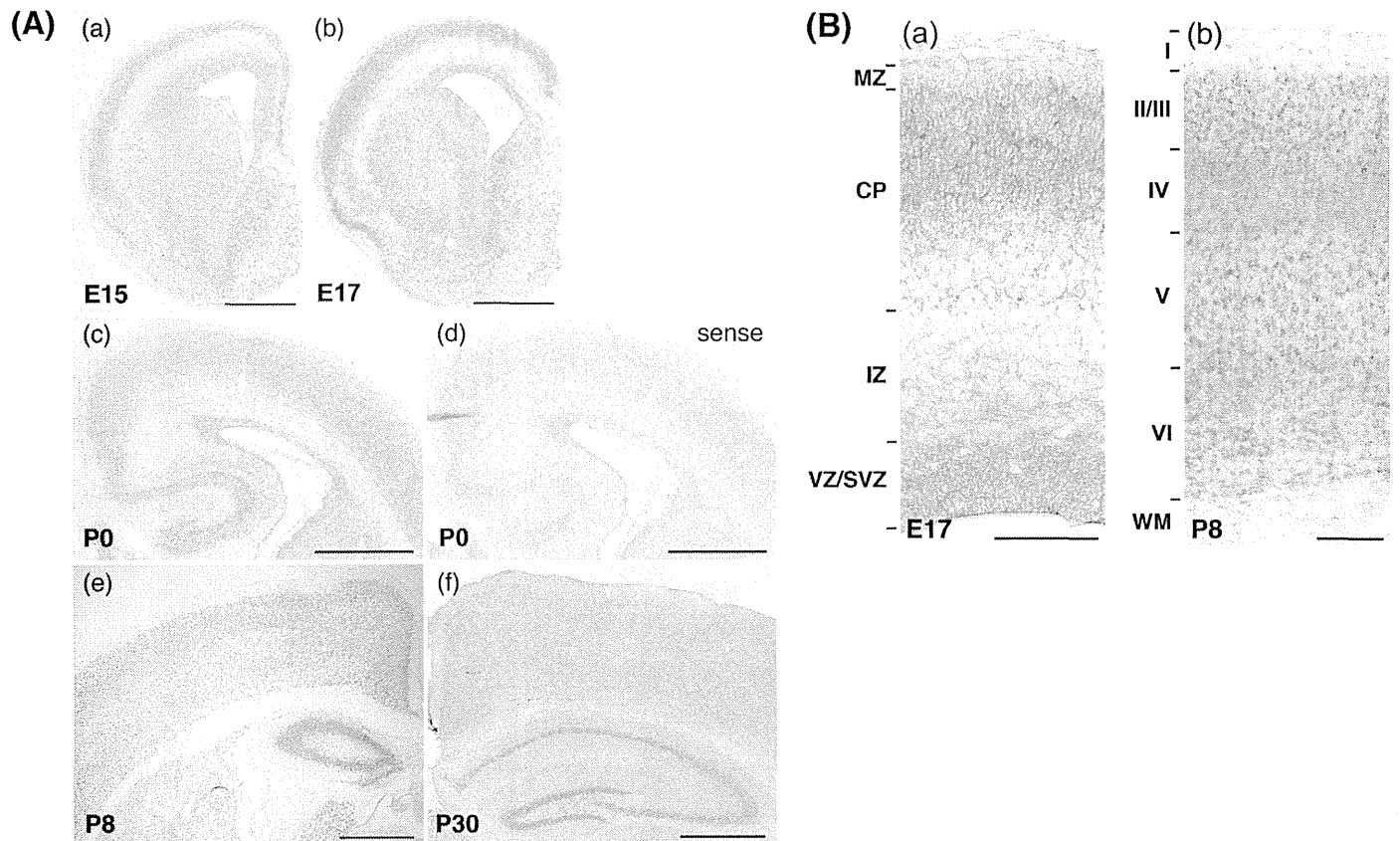
Fig. 5. In situ hybridization of Tim during mouse brain development. (A) Coronal sections were examined for Tim-mRNA expression at E15 (a), E17 (b), P0 (c), P8 (e) and P30 (f). Sense control cRNA probe was used for the P0 slice (d). Bars, 500 μm. (B) Magnified images of cerebral cortex at E17 and P8. Bars, 100 μm.

antibody with the antigen inhibited the immunoreactivity (Fig. 1A, upper right panel). Immunoreactivity of anti-Tim was significantly reduced when expression of GFP-Tim was silenced in COS7 cells by RNAi method using pSuper-Tim vector (Fig. 1B). Also, anti-Tim immunoprecipitated GFP-Tim expressed in COS7 cell lysates (Fig. 1C). From these results, we concluded that anti-Tim specifically recognized Tim.

### 3.2. Tim expression in mouse brain and cultured cell lines

Since Tim is involved in the developmental process of lung and kidney (Li et al., 2000; Xiao et al., 2003), this molecule may also play an important role in brain development. To gain some insight into the functions of Tim during neuronal development, we analyzed the expression level of Tim in the mouse brain during embryonic as well as postnatal developmental stage. As shown in Fig. 2A, one major band with ~160 kDa was visualized from embryonic day 13 (E13) to postnatal day 30 (P30), of which amount was slightly lower during the perinatal stage. This molecular mass is comparable to those reported previously with independently generated anti-Tim antibodies (Yoshizawa-Sugata and Masai, 2007; Gotter et al., 2007). On the other hand, a protein band with ~120 kDa was also visualized from E13, which gradually decreased after birth. It is not clear if this is a degradation product or yet unidentified isoform. It should be noted here that one anti-Tim antibody so far reported recognized single ~120 kDa protein in cultured cell lines such as A549, NIH3T3 and HeLa cells (Xiao et al., 2003). Relationship between the ~120 kDa protein detected in the present study and that described by Xiao et al. (2003) remains to be clarified. Meanwhile, a ~60 kDa protein was weakly detected after P15, which might be the short

isoform, Tim-S (Li et al., 2000), or a degradation product during sample preparation.

When cultured cell lines were analyzed for Tim expression in western blotting, the ~160 kDa band was detected strongly in B16 and Neuro2A cells, and only faintly in Ins-1, NIH3T3 and C6 cells (Fig. 2B). The protein bands with the molecular masses less than 55 kDa may be degradation products during sample preparation. We then did immunofluorescence analyses to examine the subcellular localization of Tim in B16 and Neuro2A cells, using a confocal microscope. In these cells, Tim was diffusely distributed throughout the cytoplasm (Fig. 2C). Tim was also present at neurites in Neuro2A cells, suggestive of some role of Tim there (Fig. 2C, lower panels).

3.3. Immunohistochemical analyses of Tim in the mouse brain developmental process

To determine the protein localization of Tim during brain development, we carried out immunohistochemical analyses. When E15 and E17 sections were stained, Tim was detected in neuronal progenitors/stem cells in ventricular zone (VZ)/subventricular zone (SVZ) as well as neurons in the cortical plate (CP) (Fig. 3A, a–c). Tim was also distributed in neurons in the CP and cerebral cortex at P0 and P8, respectively (Fig. 3A, d and e). It is notable that relative enrichment of Tim was observed in the nucleus at these time points. On the other hand, Tim immunoreactivity became diffused at P30 (Fig. 3A, d and e). Thus, we examined the intracellular distribution at E15 and P30 with magnified images. Consequently, the localization pattern was dramatically changed; Tim was relatively enriched in the nucleus of progenitor/stem

(A)

(B)

(C)
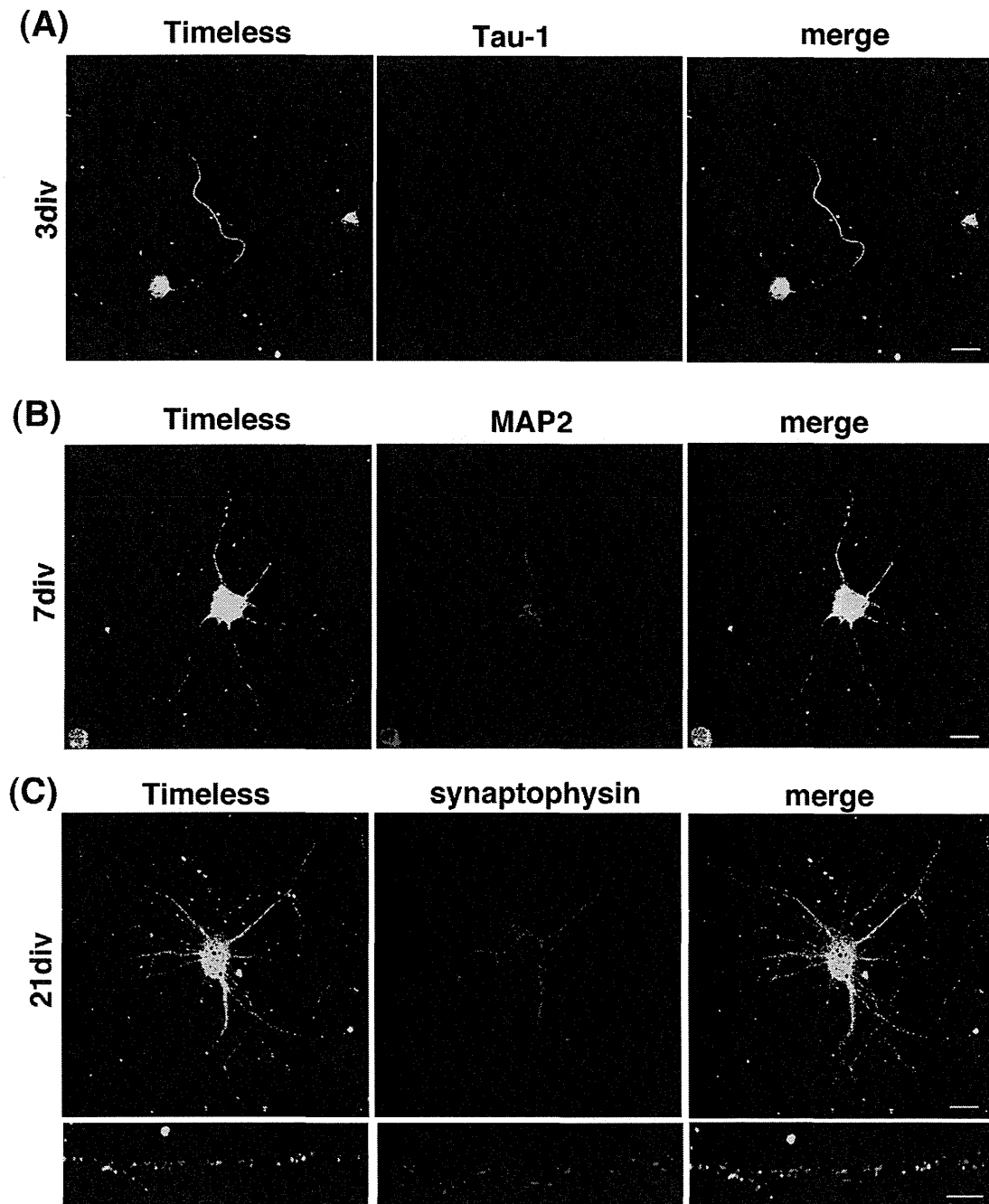
Fig. 6. Localization of Tim in primary cultured mouse hippocampal neurons. Neurons at 3 div (A), 7 div (B) and 21 div (C) were stained for Tim together with anti-Tau-1 (A), anti-MAP2 (B) or anti-synaptophysin (C), respectively. Merged images were also shown. Images of the indicated areas of upper panels in (C) were demonstrated at higher magnification as lower panels. Bars in (A), (B) and upper panel of (C), 20 μm. Bar in lower panel of (C), 5 μm.

cells in VZ/SVZ (Fig. 3B, a and b) and neurons in CP (Fig. 3B, c) at E15 while the protein was distributed in the cytoplasm of cortical neurons at P30 (Fig. 3B, d). Similar intracellular distribution profile was observed in hippocampal neurons. Tim was enriched in the nucleus of pyramidal neurons at the early stage of hippocampal formation (E17; Fig. 4A). Then, Tim immunoreactivity became weaker at P0 although the nuclear localization was still observed (Fig. 4B). Finally, Tim appeared to be excluded from nucleus and mainly distribute in the cytoplasm at P30 (Fig. 4C).

The mechanism through which Tim exerts its essential role in the CNS developmental process remains elusive. In addition to the circadian rhythm, Tim is supposed to play a role in the cell cycle checkpoint regulation by maintaining and monitoring the integrity of the DNA replication fork in the nucleus (Yoshizawa-Sugata and Masai, 2007; Gotter et al., 2007). For the nuclear localization and function of Tim, a constitutive binding partner Tipin is reported to be essential (Yoshizawa-Sugata and Masai, 2007; Gotter et al., 2007). Taken together, enrichment of Tim in the nucleus of cortical and hippocampal neurons during the brain development implies its role in cell cycle and DNA replication in a concerted manner with Tipin. On the other hand, cytoplasmic distribution of Tim in adult cortical and hippocampal neurons might reflect some role of the molecule in the circadian rhythm. We consider the antibody generated in this study will contribute to biochemical and cell biological analyses of Tim.

3.4. In situ hybridization of Tim in the mouse brain

Since Tim was intensively investigated as a circadian clock gene, mRNA expression was first examined by focusing on the clock center suprachiasmatic nucleus (SCN) in the adult mouse (Koike et al., 1998; Zylka et al., 1998; Sangoram et al., 1998; Takumi et al., 1999). In these reports, strong Tim expression was detected in SCN and pars tuberalis while moderate signals were visualized in the cingulated cortex, periventricular area of the caudate putamen, cerebellar granular cell layer. It is notable that only weak signal was detected in the cerebral cortex in adult mouse (Koike et al., 1998; Zylka et al., 1998; Sangoram et al., 1998; Takumi et al., 1999). On the other hand, when Tim expression was analyzed in embryonic mice at E14.5, the mRNA was detected strongly in branching epithelial tissues including kidney, liver and lung, and moderately in brain (Li et al., 2000).

Since detailed analyses for Tim-mRNA distribution have not been performed morphologically during brain development, we examined in situ hybridization of Tim at E15, E17, P0, P8 and P30. The mRNA was detected in CP, VZ/SVZ and ganglionic eminence at E15 and E17 (Fig. 5A, a and b). Tim-mRNA was also detected in developing hippocampus at P0 (Fig. 5A, c and d). On the other hand, the mRNA was faintly recognized in IZ during embryonic stage (Fig. 5A, a and b, and B, a). After birth, significant signal was detected in hippocampus in addition to the cortex at P8 and P30 (Fig. 5A, e and f). Magnified images of cerebral cortex were depicted in Fig. 5B; Tim-mRNA was expressed relatively strongly in cortical neurons in CP at E17, and detected throughout the cortex at P8.

3.5. Subcellular localization of Tim in primary cultured hippocampal neurons

Since Tim is expressed in a developmental stage-dependent manner in the hippocampus, it might be involved in the neuron development and functions in hippocampus. To obtain some insight into the function of Tim in differentiated hippocampal neurons, we looked into the localization of Tim in the primary cultured neurons. In immature neurons at 3 days in vitro (div) or 7div, Tim was observed in the nucleus, soma, Tau-1-positive axon and MAP2-positive dendrites (Fig. 6A and B). In matured 21 div neurons, Tim was also located in the nucleus and cytoplasm (Fig. 6C). It should be noted that Tim was distributed in a panctate pattern in processes of 21 div neurons, although the localization was not matched with a synaptic marker synaptophysin (Fig. 6C, lower panels). While subcellular localization of Tim altered during corticogenesis in immunohistochemical analyses (Fig. 4), the localization pattern did not change in the primary cultured hippocampal neurons from div3 to 21 (Fig. 6). We assume the discrepancy observed was perhaps due to the experimental conditions used in each analysis.

4. Conclusion

In the present study, we performed some biochemical and morphological characterization of Tim by the use of a homemade antibody. Tim protein was detected by Western blotting in cerebral cortex throughout the developmental stage. Immunohistochemistry revealed that Tim gradually changed its intracellular location during corticogenesis, from the nucleus to the cytoplasm in cortical neurons as well as hippocampal ones. Tim-mRNA expression profile in in situ hybridization was similar to that of the protein in immunohistochemical analyses. Although complex formation of Tim with its binding partner Tipin is thought to be crucial for nuclear localization of Tim (Yoshizawa-Sugata and Masai, 2007),

further analyses are required to elucidate the physiological relevance of the translocation of Tim during corticogenesis.

References

Ajioka, I., Maeda, T., Nakajima, K., 2006. Identification of ventricular-side-enriched molecules regulated in a stage-dependent manner during cerebral cortical development. Eur. J. Neurosci. 23, 296–308.

Gotter, A.L., 2006. A Timeless debate: resolving TIM's noncircadian roles with possible clock function. Neuroreport 17, 1229–1233.

Gotter, A.L., Suppa, C., Emanuel, B.S., 2007. Mammalian TIMELESS and Tipin are evolutionarily conserved replication fork-associated factors. J. Mol. Biol. 366, 36–52.

Gotter, A.L., Manganaro, T., Weaver, D.R., Kolakowski Jr., L.F., Possidente, B., Sriram, S., MacLaughlin, D.T., Reppert, S.M., 2000. A time-less function for mouse timeless. Nat. Neurosci. 3, 755–756.

Hanai, N., Nagata, K., Kawajiri, A., Shiromizu, T., Saitoh, N., Hasegawa, Y., Murakami, S., Inagaki, M., 2004. Biochemical and cell biological characterization of a mammalian septin, Sept11. FEBS Lett. 568, 83–88.

Ito, H., Morishita, R., Shinoda, T., Iwamoto, I., Sudo, K., Okamoto, K., Nagata, K., 2010. Dysbindin-1, WAVE2 and Abi-1 form a complex that regulates dendritic spine formation. Mol. Psychiatry 15, 976–986.

Kirihara, Y., Takechi, M., Kurosaki, K., Kobayashi, Y., Kurosawa, T., 2013. Anesthetic effects of a mixture of medetomidine, midazolam and butorphanol in two strains of mice. Exp. Anim. 62, 173–180.

Koike, N., Hida, A., Numano, R., Hirose, M., Sakaki, Y., Tei, H., 1998. Identification of the mammalian homologues of the Drosophila timeless gene, Timeless1. FEBS Lett. 441, 427–431.

Li, Z., Stuart, R.O., Qiao, J., Pavlova, A., Bush, K.T., Pohl, M., Sakurai, H., Nigam, S.K., 2000. A role for Timeless in epithelial morphogenesis during kidney development. Proc. Natl. Acad. Sci. U. S. A. 97, 10038–10043.

McFarlane, R.J., Mian, S., Dalgaard, J.Z., 2010. The many facets of the Tim-Tipin protein families' roles in chromosome biology. Cell Cycle 9, 700–705.

Murase, K., Ito, H., Kanoh, H., Sudo, K., Iwamoto, I., Morishita, R., Soubeyran, P., Seishima, M., Nagata, K., 2012. Cell biological characterization of a multi-domain adaptor protein, ArgBP2, in epithelial NMuMG cells, and identification of a novel short isoform. Med. Mol. Morphol. 45, 22–28.

Nagata, K., Ito, H., Iwamoto, I., Morishita, R., Asano, T., 2009. Interaction of a multidomain adaptor protein, vinexin, with a Rho-effector, Rhotekin. Med. Mol. Morphol. 42, 9–15.

Reppert, S.M., 1998. A clockwork explosion! Neuron 21, 1–4.

Sangoram, A.M., Saez, L., Antoch, M.P., Gekakis, N., Staknis, D., Whiteley, A., Fruechte, E.M., Vitaterna, M.H., Shimomura, K., King, D.P., Young, M.W., Weitz, C.J., Takahashi, J.S., 1998. Mammalian circadian autoregulatory loop: a Timeless ortholog and mPer1 interact and negatively regulate CLOCK-BMAL1-induced transcription. Neuron 21, 1101–1103.

Sudo, K., Ito, H., Iwamoto, I., Morishita, R., Asano, T., Nagata, K., 2006. Identification of a cell polarity-related protein, Lin-7B, as a binding partner for a Rho effector, Rhotekin, and their possible interaction in neurons. Neurosci. Res. 56, 347–355.

Takumi, T., Nagamine, Y., Miyake, S., Matsubata, C., Taguchi, K., Takekida, S., Sakakida, Y., Nishikawa, K., Kishimoto, T., Niwa, S., Okumura, K., Okamura, H., 1999. A mammalian ortholog of Drosophila timeless, highly expressed in SCN and retina, forms a complex with mPER1. Genes Cells 4, 67–75.

Unsal-Kaçmaz, K., Mullen, T.E., Kaufmann, W.K., Sancar, A., 2005. Coupling of human circadian and cell cycles by the timeless protein. Mol. Cell. Biol. 25, 3109–3116.

Xiao, J., Li, C., Zhu, N.L., Borok, Z., Minoo, P., 2003. Timeless in lung morphogenesis. Dev. Dyn. 228, 82–94.

Yoshizawa-Sugata, N., Masai, H., 2007. Human Tim/Timeless-interacting protein, Tipin, is required for efficient progression of S phase and DNA replication checkpoint. J. Biol. Chem. 282, 2729–2740.

Zylka, M.J., Shearman, L.P., Levine, J.D., Jin, X., Weaver, D.R., Reppert, S.M., 1998. Molecular analysis of mammalian Timeless. Neuron 21, 1115–1122.

ORIGINAL
ARTICLE

Role of an adaptor protein Lin-7B in brain development: possible involvement in autism spectrum disorders

Makoto Mizuno,*,[1] Ayumi Matsumoto,†,[1] Nanako Hamada,* Hidenori Ito,* Akihiko Miyauchi,† Eriko F. Jimbo,† Mariko Y. Momoi,† Hidenori Tabata,* Takanori Yamagata† and Koh-ichi Nagata*

*Department of Molecular Neurobiology, Institute for Developmental Research, Aichi Human Service Center, Kasugai, Japan

†Department of Pediatrics, Jichi Medical University, Tochigi, Japan

Abstract

Using comparative genomic hybridization analysis for an autism spectrum disorder (ASD) patient, a 73-Kb duplication at 19q13.33 (nt. 49 562 755–49 635 956) including *LIN7B* and 5 other genes was detected. We then identified a novel frameshift mutation in *LIN7B* in another ASD patient. Since *LIN7B* encodes a scaffold protein essential for neuronal function, we analyzed the role of Lin-7B in the development of cerebral cortex. Acute knockdown of Lin-7B with *in utero* electroporation caused a delay in neuronal migration during corticogenesis. When Lin-7B was knocked down in cortical neurons in one hemisphere, their axons failed to extend efficiently into the contralateral hemisphere after leaving the corpus callosum. Meanwhile, enhanced expression of Lin-7B had no effects on both cortical neuron migration and axon growth. Notably, silencing of Lin-7B did not affect the proliferation of neuronal progenitors and stem cells. Taken together, Lin-7B was found to play a pivotal role in corticogenesis through the regulation of excitatory neuron migration and interhemispheric axon growth, while further analyses are required to directly link functional defects of Lin-7B to ASD pathophysiology.

Keywords: autism, cerebral cortex, development, Lin-7B, neuronal migration.

J. Neurochem. (2015) **132**, 61–69.

Lin-7 has been reported to play a critical role as a scaffold protein in synaptic development, plasticity, and functions (Borg *et al.* 1998; Butz *et al.* 1998; Jo *et al.* 1999; Perego *et al.* 2000; Sudo *et al.* 2006). The Lin-7 family is composed of Lin-7A-C, also termed as MALS1-3 and Veli1–3 (Butz *et al.* 1998; Irie *et al.* 1999; Jo *et al.* 1999; Doerks *et al.* 2000). The molecular structure of this family is highly conserved; they share an N-terminally located PSD-95, Discs-large and ZO-1 (PDZ) domain, and a L27 domain in the C-terminal region. The L27 domain associates with membrane-associated guanylate kinase proteins such as synapse-associated protein 97, PSD93, PSD95, calcium/calmodulin-dependent serine protein kinase, and protein associated with LIN-7 (Pals), to form a heterodimer (Zheng *et al.* 2011). The PDZ domain also interacts with several proteins indispensable for neuronal cell signaling, polarity, and adhesion (Feng and Zhang 2009).

Accumulating evidence has revealed that impairment of Lin-7 function may be involved in some neuronal and developmental disorders. Polymorphisms of *LIN7* were shown to be associated with attention-deficit/hyperactivity disorder (Lanktree *et al.* 2008). Microdeletions at 11p14.1, in which *LIN7C* is located, were reported to associate with attention-deficit/hyperactivity disorder, autism spectrum

61

disorder (ASD), and developmental delay (Shinawi *et al.* 2011). In Huntington's disease, Lin-7B expression was decreased in pyramidal neurons in layer V of cerebral cortex, suggestive of impaired neuronal connectivity (Zucker *et al.* 2010). In addition, we recently proposed a pathophysiological role for Lin-7A in a 12q21-deletion syndrome with intellectual disability (ID) (Matsumoto *et al.* 2014).

In this study, we identified a 73 kb-duplication at 19q31.33 in an ASD patient (Patient #1, a 19-year-old Japanese boy), using array comparative genomic hybridization (aCGH) analysis. We focused on *LIN7B* among six genes located in the duplicated region, screened for *LIN7B* mutations in unrelated ASD patients, and found a heterozygous missense mutation (c.602+1G>C) at the donor site of exon 5 in a 26-year-old Caucasian woman (Patient #2). Since these results suggest the involvement of Lin-7B in ASD etiology, we performed *in vitro* and *ex vivo* analyses by focusing on the role of Lin-7B in cerebral cortex development. While Lin-7B did not appear to be involved in neuronal cell proliferation, Lin-7B deficiency caused defects in migration and axon growth of excitatory pyramidal neurons during corticogenesis.

Materials and methods

Ethics statement

This research was approved by the bioethics committee for human gene analysis at Jichi Medical University (approval number 11–14), and written informed consent was obtained for the genetics analyses. We followed the Fundamental Guidelines for Proper Conduct of Animal Experiments and Related Activity in Academic Research Institution under the jurisdiction of the Ministry of Education, Culture, Sports, Science and Technology, Japan. All the protocols for animal handling and treatment were reviewed and approved by the Animal Care and Use committee of Institute for Developmental Research, Aichi Human Service Center (approval number M10).

aCGH analysis

Lymphocytes were obtained from 49 unrelated Japanese patients (40 males and 9 females) who consulted Jichi Medical University Hospital; 36 patients diagnosed as ASD, 11 patients as pervasive developmental disorder (PDD) not otherwise specified (PDD-NOS), and 2 patients as Asperger syndrome by Diagnostic and Statistical Manual of Mental Disorders – IV (DSM-IV). The age of the patients ranged from 2 to 36 years. Forty patients (81.6%) had ID, and 16 patients (32.7%) had epilepsy. aCGH analysis was performed using the Agilent Human genome CGH 180K (Agilent Technologies, Santa Clara, CA, USA) essentially as described (Matsumoto *et al.* 2014).

RT-PCR and sequencing analysis

Genomic DNA was extracted using the standard method from peripheral blood lymphocytes or lymphoblasts of 83 unrelated Japanese patients (66 males and 17 females) with ASD, PDD-NOS, and Asperger syndrome according to the DSM-IV. The age of the patients ranged from 2 to 36 years. The IQ and language ability of the patients varied from severely affected to normal. All exons and exon-intron boundaries of *LIN7B* were amplified separately by PCR. The primer sequence information will be provided on request. DNA samples of 80 Caucasian patients including ASD and PDD (70 males and 10 females) were obtained from the Autism Genetic Resource Exchange (AGRE) Consortium (Cure Autism Now, Los Angeles, CA, USA). Caucasian control samples were obtained from Coriell Institute (Camden, NJ, USA).

ASD network analysis

Data of the duplicated genes in Patient #1 and genes reported to relate to ASD etiology were analyzed using Ingenuity Pathway Analysis application (http://www.ingenuity.com) (Qiagen, Hilden, Germany).

Plasmids

cDNAs encoding human (h) Lin-7B, mouse (m) Lin-7A and Lin-7B were described previously (Sudo *et al.* 2007; Matsumoto *et al.* 2014). c.602+1G>C mutant cDNA, encoding hLin-7B (p.S147VfsX30), was produced by PCR. The cDNAs were constructed into pCAG-Myc-MCS2 or pCAG-GFP-MCS2 vector (Kawauchi *et al.* 2005). All constructs were verified by DNA sequencing.

RNA interference

pSUPER-RNAi-puro vector (OligoEngine, Seattle, WA, USA) was designed to target 2 distinct coding sequences in mLin-7B cDNA (pSUPER-mLin7B-RNAi#1: 5′-GTGTATGAACAGCTCTATG-3′, 156-174; pSUPER-mLin7B-RNAi#2: 5′-TCTGTGAATGGTGT GAGTG-3′, 425-443). Numbers indicate the position from transcription start sites. As an RNAi-resistant version of mLin-7B, we used the human ortholog where the target sequences contain mismatched nucleotides (Figure S1c and d).

Primary antibodies

Polyclonal rabbit anti-GFP and anti-Myc antibodies were generated as described (Mizutani *et al.* 2013) Anti-β-tubulin (mouse monoclonal) was purchased from Sigma (Tokyo, Japan).

Cell culture, transfection, and immunofluorescence

COS7 and mouse primary cortical neurons were cultured essentially as described (Nagata *et al.* 2009; Shinoda *et al.* 2010). Cells were transfected by Lipofectamine 2000 (Life Technologies, Tokyo, Japan) according to the manufacturer's instruction. Immunofluorescence analyses were performed as described (Ito *et al.* 2010). Alexa Fluor 488- or 568-labeled IgG (Life Technologies) was used as a secondary antibody. Fluorescent images were obtained using FV-1000 confocal laser microscope (Olympus, Tokyo, Japan).

In utero electroporation

Pregnant ICR mice were purchased from SLC Japan (Shizuoka, Japan). *In utero* electroporation was performed essentially as described (Tabata and Nakajima 2001; Nishimura *et al.* 2012). Briefly, 2 μL of nucleotide solution containing expression plasmids plus pSUPER-RNAi plasmids (2 μg each) or pCAG-GFP-mLin-7B only was introduced into the lateral ventricles of embryos, followed by electroporation using CUY21 electroporator (NEPA Gene, Chiba, Japan) with 50 ms of 30 V electronic pulse for six times

with 950 ms intervals. All electroporations in this report were performed on embryonic day 14.5 (E14.5) and at least five brains were used for each experiment.

Quantitative analysis of neuronal migration and axon elongation

Three selected brains from all electroporated brains were used for this experiment. For migration analyses, the distribution of GFP-positive cells in brain slices was quantified as follows. Coronal sections of cerebral cortices containing the labeled cells were classified into four regions, layer II–IV, V–VI, intermediate zone (IZ), and the subventricular zone (SVZ)/ventricular zone (VZ), as described previously (Inaguma et al. 2014). After selecting three electroporated brains, the number of labeled cells in each region of one selected slice per each brain was calculated using ImageJ software (an open source image processing program). For estimation of axon growth, GFP signal intensity of callosal axons was measured in a 170 × 300 μm rectangle on both the ipsilateral [before entering the corpus callosum (CC)] and contralateral (after leaving the CC) sides at the positions indicated in Fig. 5(a,i). We then calculated the ratio of the ipsilateral axonal GFP signal density to that in the corresponding contralateral side using the Adobe Photoshop software (Adobe Systems Inc., San Jose, CA, USA).

EdU (5-ethynil-2′-deoxyuridine) incorporation experiments

Embryos were electroporated with pCAG-enhanced green fluorescent protein (EGFP) vector together with pSUPER-RNAi vector (control) or pSUPER-mLin7B-RNAi#1 in utero at E14. Thirty hours after electroporation, pregnant mice were given an intraperitoneal injection of EdU at 25 mg/kg body weight. One hour after the injection, embryonic brains were fixed with 4% paraformaldehyde, and vibratome sections were obtained. GFP and EdU were detected with anti-GFP and Alexa Fluor555 azide (Life Technologies), respectively, according to the manufacturer's protocols.

Statistical analysis

Results were expressed as means ± SD. When data were obtained from only two groups, Student's t-test was used for comparison. For other experiments, the rate of cell scores were initially analyzed using the one-way ANOVA. Subsequently, a Fisher's least significant difference test (LSD) was applied to absolute values as a post hoc test of multiple comparisons. The level of statistical significance was considered to be $p < 0.05$. Statistical analysis was performed using Statview software (SAS Institute, Cary, NC, USA).

Results

aCGH analysis

In the proband Patient #1, aCGH analysis detected a 73-Kb duplication at 19q13.33 (nt. 49 562 755–49 635 956) (Fig. 1a and b). aCGH analyses of the patient's parents and brother did not detect this duplication, indicating that this duplication occurred de novo (Fig. 1b). Six genes located in this duplicated region were Neurotrophin 4 (NTF4), Potassium channel, voltage-gated, shaker-related subfamily, member 7 (KCNA7), LIN7B, Chromosome 19 open reading frame 73 (C19orf73), Protein tyrosine phosphatase, receptor type f polypeptide-interacting protein alpha 3 (PPFIA3), and small

nuclear ribonucleoprotein 70 kDa (U1) (SNRNP 70) (Fig. 1c). Among these, Ingenuity Pathway Analysis revealed that LIN7B interacts directly to the ionotropic glutamate receptor, N-methyl-D-aspartate subunit 2B (GRIN2B), one of the ASD-susceptible genes (Figure S1). We thus focused on LIN7B as a possible gene implicated in ASD etiology, and performed further genetic analyses.

Sequence analysis

Since DNA duplication including LIN7B was detected in Patient #1, we screened ASD, PDD-NOS and Asperger syndrome patients for mutations in LIN7B, and identified a heterozygous missense mutation, c.602+1G>C, located at the splice-donor site of exon 5 in Patient #2 (Fig. 2A). When the mutation was further analyzed by RT-PCR to investigate the coding change in exon 5, two PCR products with ~ 150 bp and ~ 300 bp were detected in the patient while a single 300 bp-band was amplified in the control sample (Fig. 2B and C, left). Subsequent sequence analyses revealed that exon 4 directly connected with exon 6, leading to exon 5 skipping, introduction of a novel splice-donor site and frameshift at codon 147 (Fig. 2C, right). Consequently, the c.602+1G>C mutation caused the deletion of one-third of the PDZ domain from the C-terminus and premature truncation of the protein with addition of 30 novel amino acids (p.S147VfsX30) (Fig. 2B and D). This mutation has not been detected in the NCBI database and 179 control individuals. The expression pattern of p.S147VfsX30 was compared to that of wild type Lin-7B by western blotting analysis (Fig. 2E).

Roles of Lin-7B in neuronal migration during corticogenesis

To investigate whether functional defects of LIN7B induce abnormal brain development which might be related to pathophysiology of ASD, we performed RNAi experiments and examined a possible role of Lin-7B in the migration of newly generated cortical neurons. We designed 2 RNAi vectors, pSUPER–mLin7B-RNAi#1, and pSUPER–mLin7B-RNAi#2, against distinct regions in the mLin7B coding sequence. Both vectors efficiently knocked down mLin-7B expressed in COS7 cells (Figure S2a). Since mLin-7A, which is also abundant in the cerebral cortex, has structural similarity to mLin-7B, we asked whether these RNAi vectors knock down mLin-7A. Neither pSUPER–mLin7B-RNAi#1 nor –mLin7B-RNAi#2 silenced mLin-7A expressed in COS7 cells (Figure S2b), suggesting that Lin-7A expression was maintained upon Lin-7B knockdown. We next tested if pSUPER–mLin7B-RNAi#1 and –mLin7B-RNAi#2 knock down hLin-7B. hLin-7B was resistant to these RNAi vectors because of the target sequence differences (Figure S2c and d). We thus used hLin-7B in the rescue experiments.

Next, the RNAi vectors and pCAG–EGFP were co-electropolated in utero into progenitor cells in the VZ of E14.5 mice brains. When the localization of transfected cells and their progeny was analyzed at P2, control
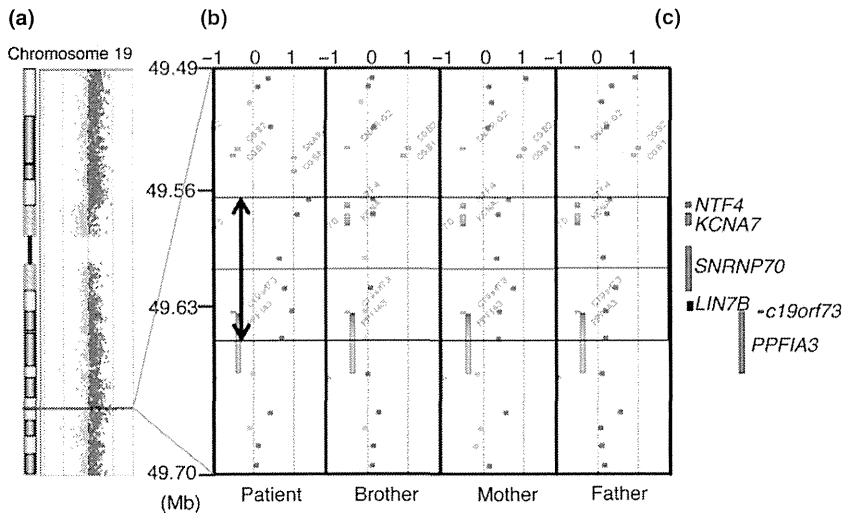
Fig. 1 Array CGH analysis of Patient #1. (a) Array CGH analysis of the entire chromosome 19 in the patient, showing a 73-kb duplication of 19q13.33. (b) Detailed views of the microarray plots for the patient, his brother, and parents. The vertical axis shows megabases (Mb) from the telomere of 19q, and the horizontal axis shows the fold-change in copy number variation. The bidirectional arrow and surrounding area show the duplication in the patient. (c) Genes present in the duplicated area.

vector-transfected neurons migrated normally to the superficial layer (layers II–IV) of the cortical plate (CP) [Fig. 3a (i)]. In contrast, cells transfected with pSUPER–mLin7B-RNAi#1 or pSUPER–mLin7B-RNAi#2 frequently remained in the lower CP and IZ [Fig. 3a(i and iii)]. One-way ANOVA clarified significant effects of both vector injections [layers II–IV ($F_{2,6}$ = 90.195, p < 0.0001); layers V–VI ($F_{2,6}$ = 50.602, p = 0.0002); IZ ($F_{2,6}$ = 101.223 p < 0.0001) and SVZ/VZ ($F_{2,6}$ = 36.881, p = 0.0004)]. *Post hoc* tests revealed significant abnormal migration in neurons transfected with pSUPER–mLin7B-RNAi#1 and #2 when compared to the control pSUPER vector (Fig. 3b).

We next examined long-term effects of Lin-7B silencing on neuron migration at P7. Notably, Lin-7B-deficient cells reached the target destination (layers II–IV) at this time point, showing that knockdown of Lin-7B delayed, but did not prevent, the radial migration of cortical neurons (data not shown). This result was similar to that of Lin-7A silencing experiments (Matsumoto *et al.* 2014). Although the molecular mechanism(s) of Lin-7 proteins in cell migration has not so far been analyzed, their regulatory roles in filopodia formation (Crespi *et al.* 2012) and endocytosis (Straight *et al.* 2001) might account for their involvement in cell migration.

Rescue experiments were conducted to rule out off-target effects. To this end, we used hLin-7B since it works as a resistant version to pSUPER–mLin7B-mediated knockdown (Figure S2c and d). When we electroporated pCAG–mCherry with pSUPER–mLin7B-RNAi#1 together with pCAG–GFP-hLin-7B, the positional defects were rescued at P2 [Fig. 4a(i–iii)]. It is notable that GFP-hLin-7B (p.S147VfsX30) could not rescue the phenotype under the conditions where hLin-7B could [Fig. 4a(iv)]. One-way ANOVA demonstrated significant effects of co-transfection with pCAG–GFP-hLin-7B or hLin-7B(p.S147VfsX30) [layers II–IV ($F_{2,6}$ = 36.357, p = 0.0004); layers V–VI ($F_{2,6}$ =

37.899, p = 0.0004); IZ ($F_{2,6}$ = 11.368, p = 0.0091) and SVZ/VZ ($F_{2,6}$ = 7.334, p = 0.0245)] (Fig. 4b). *Post hoc* tests showed significant rescue effects of abnormal migration. In sharp contrast, *post hoc* tests revealed that abnormal migration was not significantly rescued by hLin-7B (p.S147VfsX30), when compared to hLin-7B. Taken together, the obtained results pointed to a pathophysiological importance of the c.602+1G>C mutation. Functional defects in Lin-7B might disrupt cortical neuron migration, thus causing abnormal cortical architecture with possible functional implications in neurodevelopmental disorders.

Lin-7B does not regulate neuronal progenitor proliferation

Since prolonged cell cycle is accepted to result in neuronal migration delay (Reiner and Sapir 2009), we analyzed whether Lin-7B knockdown affects the proliferation of progenitor and stem cells in the VZ. For this purpose, we analyzed the effect of pSUPER–mLin7B-RNAi#1 on the cell cycle of VZ progenitor and stem cells. We labeled S-phase cells with EdU in order to detect DNA replication. Consequently, the cell cycle-G1 progression rate did not statistically differ between the control and Lin-7B-deficient cells since the deficient cells entered S-phase to a similar extent as the control cells (Figure S3a and b). Also, Lin-7B knockdown did not affect the positioning of EdU/EGFP double-positive cells in VZ and SVZ (Figure S3a). Collectively, we concluded that Lin-7B silencing did not affect the proliferation rate at VZ and SVZ, and that neuronal positioning defects observed were attributable to abnormalities in cell migration.

Involvement of Lin-7B in the interhemispheric connection of cortical neurons *in vivo*
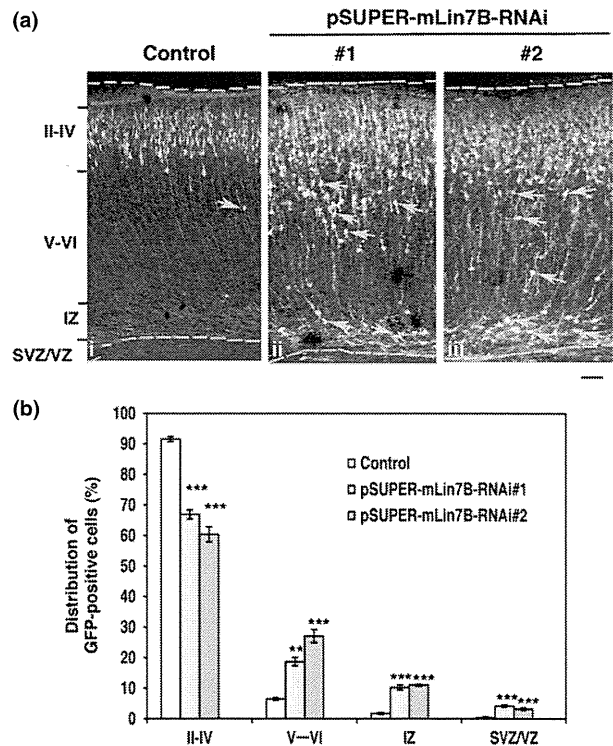
A multitude of different factors are believed to combine to produce the ASD clinical phenotypes. Given that many genes involved in synapse formation or pruning during brain
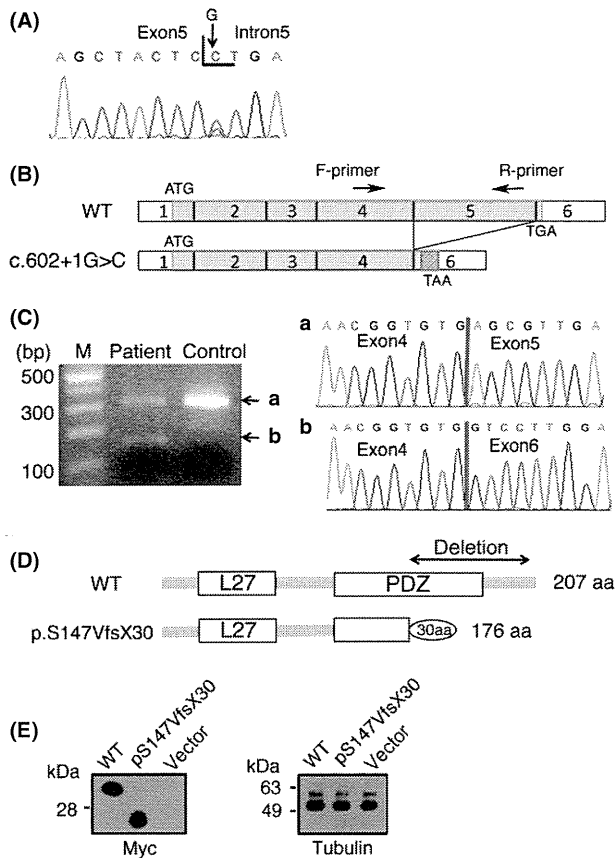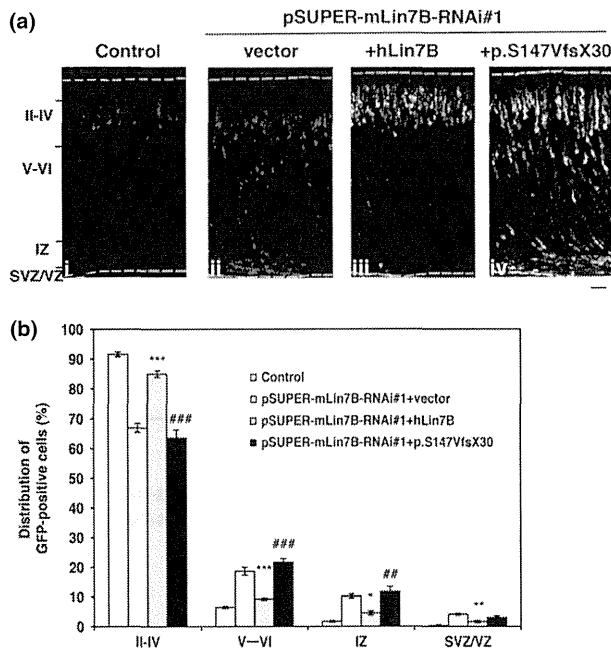
Fig. 2 Sequence analysis of Patient #2. (A) Genomic DNA sequence chromatogram. The position of the c.602+1G>C mutation is indicated. (B) Strategy of RT-PCR analysis of a normal control (WT) and c.602+1G>C mutation. (C) Two PCR products were detected from the patient's cDNA: the upper band (a, ~ 300 bp) is the wild type transcript and the lower one (b, ~ 150 bp) is the mutant transcript. The single wild type amplicon was solely detected in the control (left panel). Sequence chromatograms of wild type (a) and the mutant (b) amplicons are shown (right panels). Exon 5 skipping was detected in the mutant allele (b). (D) Schematic representation of the structure of hLin-7B (p.S147VfsX30). One third of the C-terminal PDZ domain is lacking, with additional 30 amino acids present. (E) Expression of exogenous myc-tagged hLin-7B and hLin-7B(p.S147VfsX30) in COS7 cells. Forty-eight hours after transfection, cells were harvested and subjected to western blotting (20 μg protein per lane) with anti-Myc. Tubulin was visualized as loading control.

Fig. 3 Effects of Lin-7B knockdown on neuronal migration during corticogenesis. (a) pCAG-enhanced green fluorescent protein was co-electroporated with pSUPER-RNAi vector (i), pSUPER-mLin7B-RNAi #1 (ii) or pSUPER-mLin7B-RNAi #2 (iii) into cerebral cortices at E14.5. Coronal sections were prepared at P2 and immunostained with anti-GFP (white). Nuclei were stained with DAPI (blue). Some cells in layer V–VI and IZ are marked by yellow arrows. Bar, 100 μm. (b) Quantification of the distribution of GFP-positive neurons in distinct regions of the cerebral cortex for each condition shown in (a). Error bars indicate SD ($n = 3$); ***$p < 0.0001$ (layers II–IV; control vs. mLin7B-RNAi#1), ***$p < 0.0001$ (layers II–IV; control vs. mLin7B-RNAi#2), **$p = 0.001$ (layers V–VI; control vs. mLin7B-RNAi#1), ***$p < 0.0001$ (layers V–VI; control vs. mLin7B-RNAi#2), ***$p < 0.0001$ (IZ; control vs. mLin7B-RNAi#1), ***$p < 0.0001$ (IZ; control vs. mLin7B-RNAi#2), ***$p = 0.0002$ (subventricular zone (SVZ)/ventricular zone (VZ); control vs. mLin7B-RNAi#1), ***$p = 0.0008$ (SVZ/VZ; control vs. mLin7B-RNAi#2) by Fisher's LSD.

development are considered to be linked to ASD pathophysiology (Spooren *et al.* 2012), c.602+1G>C mutation in *LIN7B* could potentially affect not only cortical neuron migration but also axon elongation and synapse network formation during corticogenesis. We thus analyzed inter-hemispheric axon projections of Lin-7B-deficient cortical neurons. When Lin-7B was silenced in VZ progenitor and stem cells at E14.5 and axons in the contralateral hemisphere were visualized at P7, the density of axons of Lin-7B-deficient neurons became lower after leaving the CC when compared to control cells; the ratio of GFP-labeled fibers was significantly decreased in the white matter of pSUPER-mLin7B-RNAi#1-transfected cortical slices [Fig. 5a(i and ii)]. This phenotype was rescued by exogenous hLin-7B [(Fig. 5a(iii)]. One-way ANOVA indicated significant effects of the RNAi vector transfection on the ratio of axon growth ($F_{2,6} = 16.519$, $p = 0.0036$) (Fig. 5b). *Post hoc* tests detected significantly reduced axon growth in Lin-7B-deficient neurons when compared to the control phenotype. Taken together, Lin-7B is likely to be required for axon growth of excitatory neurons from the ipsilateral cortex to the contralateral one, disturbance of which might lead to defects in axon/synapse network formation.

(a)

pSUPER-mLin7B-RNAi#1

Control   vector   +hLin7B   +p.S147VfsX30

II–IV

V–VI

IZ

SVZ/VZ

(b)

Distribution of GFP-positive cells (%)

□ Control
□ pSUPER-mLin7B-RNAi#1+vector
□ pSUPER-mLin7B-RNAi#1+hLin7B
■ pSUPER-mLin7B-RNAi#1+p.S147VfsX30

II–IV   V—VI   IZ   SVZ/VZ

Fig. 4 Rescue experiments of Lin-7B knockdown. (a) pCAG-mCherry was co-electroporated with pSUPER-RNAi vector only (i) or pSUPER-mLin7B-RNAi#1 together with pCAG vector (ii), pCAG-GFP-hLin-7B (iii) or -hLin-7B(p.S147VfsX30) (iv) into cerebral cortices at E14, followed by fixation at P2. Coronal sections were stained for mCherry (red), GFP (green), and nuclei (blue). Dotted lines represent the pial and ventricular surfaces. Bar, 100 μm. Cells expressing both mCherry and GFP-protein were visualized as yellow. (b) Quantification of the distribution of GFP-positive neurons in distinct regions of the cerebral cortex for each condition shown in (a). Error bars indicate SD (n = 3); ***p = 0.0005 (layers II–IV; +vector vs. +hLin-7B), ###p = 0.0002 (layers II–IV; +hLin-7B vs. +p.S147VfsX30), ***p = 0.0007 (layers V–VI; +vector vs. +hLin-7B), ###p = 0.0002 (layers V–VI; +hLin-7B vs. +p.S147VfsX30), *p = 0.0116 (layer IZ; +vector vs. +hLin-7B), ##p = 0.004 (layer IZ; +hLin-7B vs. +p.S147VfsX30), **p = 0.0087 (layer subventricular zone (SVZ)/ventricular zone (VZ); +vector vs. +hLin-7B), by Fisher's LSD.

Enhanced expression of Lin-7B is not sufficient to cause defects in neuronal migration and axon elongation

Since the 73K-duplication region in 19q13.33 detected in Patient#1 includes *LIN7B*, its higher gene dosage could induce abnormal cortical neuron migration and axon growth. We thus looked into the effects of Lin-7B over-expression on neuronal migration and intrahemispheric axon elongation. However, expression of GFP-Lin-7B had no effects on neuronal cell migration and axon growth (Figure S4).

Discussion

The molecular mechanisms underlying the etiology of neurodevelopmental disorders such as ASD are enigmatic. While we identified Lin-7B as a candidate causative gene for ASD based on aCGH and sequence analyses at the beginning

of the present study, subsequent experimental results have not necessarily supported the hypothesis that *LIN7B* is a causative gene for ASD as mentioned below. First, over-expression experiments, which should mimic *LIN7B* gene duplication in Patient#1, had no effects on neuronal migration and axon growth. However, *LIN7B* duplication could affect other important processes such as synaptogenesis and synaptic plasticity, which have not been evaluated in the present study. For this reason, further analyses will be required to determine the pathophysiological significance of *LIN7B* duplication. Secondly, the mother of Patient#2 also has the c.602+1G>C mutation (data not shown), and no information is available on whether she displays any autistic symptoms/features. This could raise a possibility that the *Lin7B* mutation is benign. In addition, it will be essential to elucidate yet unidentified additional genetic and/or environmental factor(s) to fully determine the significance of the *LIN7B* mutation in ASD etiology. Nevertheless, the results obtained from a series of cell biological analyses in this study strongly suggest that Lin-7B is involved in the process of cerebral cortex development.

In our Lin-7B-knockdown experiments, the neuronal migration delay detected at P2 recovered at P7, and these neurons eventually reached the correct target location. Such recovery was also observed in the case of silencing of Lin-7A, a possible causative gene for 12q21-deletion syndrome which has ID as a major symptom (Matsumoto *et al.* 2014). Although it remains to be clarified whether and how neuronal migration delay is crucial for neurodevelopmental disorders including ASD, it is likely that the abnormal migration process *per se* causes impairment in neuronal network formation and functions.

Differently from wild type hLin-7B, hLin-7B (p.S147VfsX30) could not rescue the migration defects caused by Lin-7B-knockdown. Since the Lin-7B PDZ domain is known to associate with several proteins (Feng and Zhang 2009), hLin-7B(p.S147VfsX30) lacking this crucial domain may be unable to interact with one or more of these important binding partner(s). As a result, this failed interaction may impair signaling pathway(s) crucial for neuronal migration and axon elongation during corticogenesis. Alternatively, the L27 domain-mediated signal transduction might be abrogated by a dominant negative effect of the mutated Lin-7B, and therefore the interaction of the remaining normal Lin-7B with its physiological binding partners might be inhibited in haploinsufficiency conditions.

Synapse network formation is crucial for brain development. Since Lin-7B is considered to regulate synaptogenesis and synaptic plasticity (Butz *et al.* 1998; Jo *et al.* 1999; Sudo *et al.* 2006), the *LIN7B* mutation may cause synaptic dysfunction underlying neurodevelopmental disorders. Consistently, interhemispheric axon projections were hindered when Lin-7B was silenced in the developing mouse cerebral cortex. It remains to be elucidated if interhemispheric

(a)

(b)

Fig. 5 Effects of Lin-7B knockdown on axon growth *ex vivo*. (a) Lin-7B-deficiency affects cortical axon growth. pCAG-enhanced green fluorescent protein was co-electroporated with control pSUPER-RNAi vector (i), pSUPER-mLin7B-RNAi#1 (ii) or pSUPER-mLin7B-RNAi#1 plus pCAG-Myc-hLin-7B (iii) into cerebral cortices at E14. Coronal sections were prepared at P7 and immunostained with anti-GFP (white). Bar, 1 mm. (b) Quantitative analysis of the ratio of the intensity of GFP-positive axons in the areas (red) of mLin-7B-deficient contralateral cortex to that in the area of ipsilateral cortex in (a). Error bars indicate SD ($n = 3$); $**p = 0.0013$ (control vs. pSuper-Lin7B-RNAi#1), $^\#p = 0.0124$ (pSuper-Lin7B-RNAi#1 vs. pSuper-Lin7B-RNAi#1+hLin-7B) by Fisher's LSD.
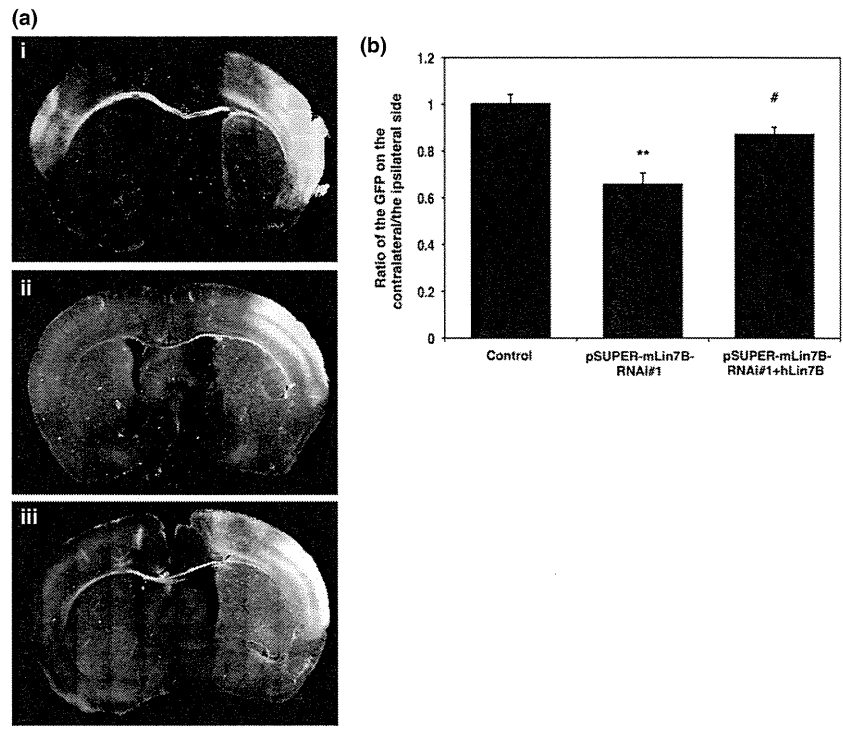
neuronal network defects really occur in patients with defective Lin-7B function, and, if so, how the abnormality determines the clinical features. In this context, the axon growth defects in Lin-7B-deficient neurons observed at P7 were because of developmental delay since these axons were extended apparently 'correctly' and arborized eventually in the contralateral cortex at P30 (data not shown). As is the case of migration delay, it is likely that the abnormal axon growth *per se* may cause deficiency in brain functions. Although enhanced expression had no effects on neuronal migration and axon growth, higher gene dosage of Lin-7B may affect synaptogenesis and/or synaptic functions.

Acute knockdown by *in utero* electroporation can circumvent the compensatory effects of general gene-knockout approaches; indeed, knockout mice for *Doublecortin* (a causative gene for subcortical band heterotopia encoding a scaffold protein), *Sept4* (encoding a cytoskeleton-related molecule related to Parkinson's disease etiology), and *Sil1* (a causative gene for Marinesco–Sjogren syndrome encoding a co-chaperone)-deficient mice exhibit no obvious morphological alteration in the cerebral cortex (Corbo *et al.* 2002; Zhao *et al.* 2005; Ihara *et al.* 2007) while acute knockdown of these genes results in defective neuronal migration (Bai *et al.* 2003; Shinoda *et al.* 2010; Inaguma *et al.* 2014). Like these mice, Lin-7A/B-double knockout mice did not show morphological alteration in cerebral cortex at the adult stage (Misawa *et al.* 2001). Based on the results obtained in this study and those described recently (Matsumoto *et al.* 2014), neuronal migration defects might take place in a transient

manner in Lin-7A/B-double knockout mice; these neurons may finally make it to their correct destination. In addition, axonal growth may also be delayed during brain development in Lin-7A/B-double knockout mice, as in the case of *in utero* electroporation-based acute silencing experiments carried out in this study.

Since the cDNAs of Lin-7A-C encode proteins that share ~ 70% identity with each other, these proteins may compensate mutually for their functions. Indeed, in the Lin-7A/B-double knockout mice, Lin-7C expression was up-regulated in the hippocampus dentate gyrus and CA1 area, which normally express Lin-7A and Lin-7B, respectively (Misawa *et al.* 2001). Although Lin-7C is expressed mainly in the olfactory bulb and cerebellum in adult mouse (Misawa *et al.* 2001), this molecule could at least partially compensate for the function of Lin-7A and/or Lin-7B during corticogenesis in the Lin-7A/B double knockout animals. The potential role of Lin-7C in corticogenesis remains to be fully elucidated.

From the results of this study, Lin-7B appears to be involved in corticogenesis. Meanwhile, the study of a 12q21-deletion syndrome patient with ID revealed that Lin-7A also plays an important role in cortical neuron migration and axon network formation during corticogenesis (Matsumoto *et al.* 2014). While both Lin-7A and Lin-7B are very likely to play a role in corticogenesis, the signaling pathways involved may be distinct since in our hands knockdown of Lin-7A and Lin-7B did not affect expression levels of Lin-7B and Lin-7A, respectively. In addition, the effect of Lin-7A knockdown on neuronal migration was more severe than that of Lin-7B

knockdown (Matsumoto *et al.* 2014). These results suggest that the functions of Lin-7A and Lin-7B may be maintained independently in neurons. Although both Lin-7A and Lin-7B seemingly engage in cerebral cortex formation, the signaling pathways involving these two proteins and the functional role of them in the formation of the neuronal network remain to be clarified.

Collectively, the present study suggests that Lin-7B takes part in corticogenesis and that its functional defects might be implicated in pathophysiology of neurodevelopmental disorders such as ASD. Further genetic and cell biological analyses will be required to fully address this possibility. Lin-7A and Lin-7B might contribute to cortical development in a coordinate manner through distinct signaling pathways converging on common regulatory steps important for neuronal migration and axon elongation.

Acknowledgments and conflict of interest disclosure

Supporting information

Additional supporting information may be found in the online version of this article at the publisher's web-site:

Figure S1. ASD network analysis using Ingenuity Pathway Analysis.

Figure S2. Characterization of pSUPER-mLin7B-RNAi vectors.

Figure S3. Effects of Lin-7B-silencing on the DNA replication in S-phase of the cell cycle.

Figure S4. Effects of enhanced expression of Lin-7B on neuronal migration and axon growth *ex vivo*.

References

Bai J., Ramos R. L., Ackman J. B., Thomas A. M., Lee R. V. and LoTurco J. J. (2003) RNAi reveals doublecortin is required for radial migration in rat neocortex. *Nat. Neurosci.* **6**, 1277–1283.

Borg J. P., Straight S. W., Kaech S. M., de Taddéo-Borg M., Kroon D. E., Karnak D., Turner R. S., Kim S. K. and Margolis B. (1998) Identification of an evolutionarily conserved heterotrimeric protein complex involved in protein targeting. *J. Biol. Chem.* **273**, 31633–31636.

Butz S., Okamoto M. and Sudhof T. C. (1998) A tripartite protein complex with the potential to couple synaptic vesicle exocytosis to cell adhesion in brain. *Cell* **94**, 773–782.

Corbo J. C., Deuel T. A., Long J. M., LaPorte P., Tsai E., Wynshaw-Boris A. and Walsh C. A. (2002) Doublecortin is required in mice for lamination of the hippocampus but not the neocortex. *J. Neurosci.* **22**, 7548–7557.

Crespi A., Ferrari I., Lonati P., Disanza A., Fornasari D., Scita G., Padovano V. and Pietrini G. (2012) LIN7 regulates the filopodium- and neurite-promoting activity of IRSp53. *J. Cell Sci.* **125**, 4543–4554.

Doerks T., Bork P., Kamberov E., Makarova O., Muecke S. and Margolis B. (2000) L27, a novel heterodimerization domain in receptor targeting proteins Lin-2 and Lin-7. *Trends Biochem. Sci.* **25**, 317–318.

Feng W. and Zhang M. (2009) Organization and dynamics of PDZ-domain-related supramodules in the postsynaptic density. *Nat. Rev. Neurosci.* **10**, 87–99.

Ihara M., Yamasaki N., Hagiwara A. *et al.* (2007) Sept4, a component of presynaptic scaffold and Lewy bodies, is required for the suppression of alpha-synuclein neurotoxicity. *Neuron* **53**, 519–533.

Inaguma Y., Hamada N., Tabata H. *et al.* (2014) SIL1, a causative cochaperone gene of Marinesco-Söjgren syndrome, plays an essential role in establishing the architecture of the developing cerebral cortex. *EMBO Mol. Med.* **6**, 414–429.

Irie M., Hata Y., Deguchi M., Ide N., Hirao K., Yao I., Nishioka H. and Takai Y. (1999) Isolation and characterization of mammalian homologues of Caenorhabditis elegans lin-7: localization at cell-cell junctions. *Oncogene* **18**, 2811–2817.

Ito H., Morishita R., Shinoda T., Iwamoto I., Sudo K., Okamoto K. and Nagata K. (2010) Dysbindin-1, WAVE2 and Abi-1 form a complex that regulates dendritic spine formation. *Mol. Psychiatry* **15**, 976–986.

Jo K., Derin R., Li M. and Bredt D. S. (1999) Characterization of MALS/Velis-1, -2, and -3: a family of mammalian LIN-7 homologs enriched at brain synapses in association with the postsynaptic density-95/NMDA receptor postsynaptic complex. *J. Neurosci.* **19**, 4189–4199.

Kawauchi T., Chihama K., Nishimura Y. V., Nabeshima Y. and Hoshino M. (2005) MAP1B phosphorylation is differentially regulated by Cdk5/p35, Cdk5/p25, and JNK. *Biochem. Biophys. Res. Commun.* **331**, 50–55.

Lanktree M., Squassina A., Krinsky M., Strauss J., Jain U., Macciardi F., Kennedy J. L. and Muglia P. (2008) Association study of brain-derived neurotrophic factor (BDNF) and LIN-7 homolog (LIN-7) genes with adult attention-deficit/hyperactivity disorder. *Am. J. Med. Genet. B Neuropsychiatr. Genet.* **147B**, 945–951.

Matsumoto A., Mizuno M., Hamada N., Nozaki Y., Jimbo F. E., Momoi Y. M., Nagata K. and Yamagata T. (2014) LIN7A depletion disrupts cerebral cortex development, contributing to intellectual disability in 12q21-deletion syndrome. *PLoS ONE* **9**, e92695.

Misawa H., Kawasaki Y., Mellor J., Sweeney N., Jo K., Nicoll R. A. and Bredt D. S. (2001) Contrasting localizations of MALS/LIN-7 PDZ proteins in brain and molecular compensation in knockout mice. *J. Biol. Chem.* **276**, 9264–9272.

Mizutani Y., Ito H., Iwamoto I., Morishita R., Kanoh H., Seishima M. and Nagata K. (2013) Possible role of a septin, SEPT1, in spreading in squamous cell carcinoma DJM-1 cells. *Biol. Chem.* **394**, 281–290.

Nagata K., Ito H., Iwamoto I., Morishita R. and Asano T. (2009) Interaction of a multi-domain adaptor protein, vinexin, with a Rho-effector, Rhotekin. *Med. Mol. Morphol.* **42**, 9–15.

Nishimura V. Y., Shinoda T., Ito H. and Nagata K. (2012) Application of in utero electroporation and live imaging in the analyses of neuronal migration during mouse brain development. *Med. Mol. Morphol.* **45**, 1–6.

Perego C., Vanoni C., Massari S., Longhi R. and Pietrini G. (2000) Mammalian LIN-7 PDZ proteins associate with beta-catenin at the cell-cell junctions of epithelia and neurons. *EMBO J.* **19**, 3978–3989.

Reiner O. and Sapir T. (2009) Polarity regulation in migrating neurons in the cortex. *Mol. Neurobiol.* **40**, 1–14.

Shinawi M., Sahoo T., Maranda B. *et al.* (2011) 11p14.1 microdeletions associated with ADHD, autism, developmental delay, and obesity. *Am. J. Med. Genet. A.* **155A**, 1272–1280.

Shinoda T., Ito H., Sudo K., Iwamoto I., Morishita R. and Nagata K. (2010) Septin 14 is involved in cortical neuronal migration via interaction with Septin 4. *Mol. Biol. Cell* **21**, 1324–1334.

Spooren W., Lindemann L., Ghosh A. and Santarelli L. (2012) Synapse dysfunction in autism: a molecular medicine approach to drug discovery in neurodevelopmental disorders. *Trends Pharmacol. Sci.* **33**, 669–684.

Straight S. W., Chen L., Karnak D. and Margolis B. (2001) Interaction with mLin-7 alters the targeting of endocytosed transmembrane proteins in mammalian epithelial cells. *Mol. Biol. Cell* **12**, 1329–1340.

Sudo K., Ito H., Iwamoto I., Morishita R., Asano T. and Nagata K. (2006) Identification of a cell polarity-related protein, Lin-7B, as a binding partner for a Rho effector, Rhotekin, and their possible interaction in neurons. *Neurosci. Res.* **56**, 347–355.

Sudo K., Ito H., Iwamoto I., Morishita R., Asano T. and Nagata K. (2007) SEPT9 sequence alterations causing hereditary neuralgic amyotrophy are associated with altered interactions with SEPT4/11 and resistance to Rho/Rhotekin-signaling. *Hum. Mut.* **28**, 1005–1013.

Tabata H. and Nakajima K. (2001) Efficient in utero gene transfer system to the developing mouse brain using electroporation: visualization of neuronal migration in the developing cortex. *Neuroscience* **103**, 865–872.

Zhao L., Longo-Guess C., Harris B. S., Lee J.-W. and Ackerman S. L. (2005) Protein accumulation and neurodegeneration in the woozy mutant mouse is caused by disruption of SIL1, a cochaperone of BiP. *Nat. Genet.* **37**, 974–979.

Zheng C. Y., Seabold G. K., Horak M. and Petralia R. S. (2011) MAGUKs, synaptic development, and synaptic plasticity. *Neuroscientist* **17**, 493–512.

Zucker B., Kama J. A., Kuhn A. *et al.* (2010) Decreased Lin7b expression in layer 5 pyramidal neurons may contribute to impaired corticostriatal connectivity in huntington disease. *J. Neuropathol. Exp. Neurol.* **69**, 880–895.

RESEARCH PAPER

New *MT-ND6* and *NDUFA1* mutations in mitochondrial respiratory chain disorders

Natsumi Uehara[1,2], Masato Mori[3], Yoshimi Tokuzawa[1], Yosuke Mizuno[1], Shunsuke Tamaru[1], Masakazu Kohda[1,4], Yohsuke Moriyama[1], Yutaka Nakachi[1,4], Nana Matoba[4], Tetsuro Sakai[5], Taro Yamazaki[5], Hiroko Harashima[5], Kei Murayama[6], Keisuke Hattori[7], Jun-Ichi Hayashi[7], Takanori Yamagata[3], Yasunori Fujita[8], Masafumi Ito[8], Masashi Tanaka[9], Ken-ichi Nibu[2], Akira Ohtake[5] & Yasushi Okazaki[1,4]

[1]Division of Functional Genomics & Systems Medicine, Research Center for Genomic Medicine, Saitama Medical University, Hidaka, Japan
[2]Department of Otolaryngology-Head and Neck Surgery, Kobe University Graduate School of Medicine, Kobe, Japan
[3]Department of Pediatrics, Jichi Medical University, Shimotsuke, Japan
[4]Division of Translational Research, Research Center for Genomic Medicine, Saitama Medical University, Hidaka, Japan
[5]Department of Pediatrics, Faculty of Medicine, Saitama Medical University, Moroyama-machi, Japan
[6]Department of Metabolism, Chiba Children's Hospital, Chiba, Japan
[7]Faculty of Life and Environmental Sciences, University of Tsukuba, Tsukuba, Japan
[8]Research Team for Mechanism of Aging, Tokyo Metropolitan Institute of Gerontology, Itabashi, Japan
[9]Department of Genomics for Longevity and Health, Tokyo Metropolitan Institute of Gerontology, Itabashi, Japan

Correspondence

Yasushi Okazaki, Division of Functional Genomics & Systems Medicine, Research Center for Genomic Medicine, Saitama Medical University, 1397-1 Yamane, Hidaka, Saitama 350-1241, Japan. Tel: +81-42-984-0448; Fax: +81-42-984-0449; E-mail: okazaki@saitama-med.ac.jp
Akira Ohtake, Department of Pediatrics, Faculty of Medicine, Saitama Medical University, 38 Morohongo, Moroyama-machi, Iruma-gun, Saitama 350-0495, Japan. Tel: +81-49-276-1220; Fax: +81-49-276-1790; E-mail: akira_oh@saitama-med.ac.jp

Abstract

Objective: Mitochondrial respiratory chain disorder (MRCD) is an intractable disease of infants with variable clinical symptoms. Our goal was to identify the causative mutations in MRCD patients. **Methods:** The subjects were 90 children diagnosed with MRCD by enzyme assay. We analyzed whole mitochondrial DNA (mtDNA) sequences. A cybrid study was performed in two patients. Whole exome sequencing was performed for one of these two patients whose mtDNA variant was confirmed as non-pathogenic. **Results:** Whole mtDNA sequences identified 29 mtDNA variants in 29 patients (13 were previously reported, the other 13 variants and three deletions were novel). The remaining 61 patients had no pathogenic mutations in their mtDNA. Of the 13 patients harboring unreported mtDNA variants, we excluded seven variants by manual curation. Of the remaining six variants, we selected two Leigh syndrome patients whose mitochondrial enzyme activity was decreased in their fibroblasts and performed a cybrid study. We confirmed that m.14439G>A (*MT-ND6*) was pathogenic, while m.1356A>G (*mitochondrial 12S rRNA*) was shown to be a non-pathogenic polymorphism. Exome sequencing and a complementation study of the latter patient identified a novel c.55C>T hemizygous missense mutation in the nuclear-encoded gene *NDUFA1*. **Interpretation:** Our results demonstrate that it is important to perform whole mtDNA sequencing rather than only typing reported mutations. Cybrid assays are also useful to diagnose the pathogenicity of mtDNA variants, and whole exome sequencing is a powerful tool to diagnose nuclear gene mutations as molecular diagnosis can provide a lead to appropriate genetic counseling.

361

Introduction

The mitochondrial respiratory chain (RC) is a pathway for vital energy generation in which ATP is generated as a form of energy by the substrates generated from glycolysis and β-oxidation. The pathway is composed of five multi-enzyme complexes (complexes I–V), two electron carriers, a quinone (coenzyme Q), and a small hem-containing protein (cytochrome c) that are located in the inner mitochondrial membrane. These RC complexes are formed from subunits encoded by both mitochondrial DNA (mtDNA) and nuclear DNA (nDNA), with the exception of complex II, which is entirely encoded by nDNA.

mtDNA is a circular double-stranded DNA molecule ~16 kb in length that encodes 37 genes comprising 13 proteins, 22 mitochondrial tRNAs, and 2 rRNAs.[1,2] Defects in mitochondrial function are associated with numerous neurodegenerative diseases, such as Parkinson's disease, Alzheimer's disease, and Huntington's disease, and, in particular with mitochondrial respiratory chain disorder (MRCD). MRCD is genetically, clinically, and biochemically heterogeneous, and it can give rise to any symptoms, in any organs or tissues, at any age and with any mode of inheritance.[3] One in 5000 births is a conservative realistic estimate for the minimum birth prevalence of MRCD.[4] Especially in children, MRCD is an intractable disease and can be regarded as the most common group of inborn errors of metabolism.[5,6]

Some MRCD patients have typical clinical findings that are caused by specific point mutations or large deletions of mtDNA. Typical clinical features include mitochondrial myopathy, encephalopathy, lactic acidosis, and stroke-like episodes (MELAS), myoclonus epilepsy associated with ragged-red fibers (MERRF), Leber's hereditary optic neuropathy (LHON), and chronic progressive external ophthalmoplegia (CPEO).[2] Although mtDNA mutations or deletions are usually found in adults showing typical clinical findings, they account for only a minority of children with MRCD. Therefore, the diagnosis of MRCD in children by screening known mtDNA mutations is rather difficult.[7] Hence, a combination of general biochemical study, histological study, and genetic analysis is essential for the diagnosis of MRCD, especially in children.[6]

In this study, we performed whole mtDNA sequencing for 90 children diagnosed with MRCD by RC enzyme assay with the aim of identifying causative mtDNA mutations.

Subjects, Materials, and Methods

Patients

Ninety Japanese pediatric patients diagnosed with MRCD and without characteristic clinical syndromes were studied. The primary diagnosis for these patients was definite or probable MRCD based on the criteria of Bernier et al.,[8] and a mitochondrial RC residual enzyme activity of <20% in a tissue, <30% in a fibroblast cell line, or <30% in two or more tissues (Data S1). Informed consent was obtained from the patients and their families before participation in the study.

Patient summaries are shown in Tables 1, 2. The details of the two patients studied in the cybrid assay are as follows: Patient (Pt) 377 is a 1-year-old girl born after a normal pregnancy to non-consanguineous parents. She has a normal brother and sister. She was hospitalized with gait difficulties at the age of 1 year. Blood lactate levels were high. Brain magnetic resonance imaging (MRI)

Table 1. Distribution of mtDNA variants and clinical features.

Characteristics		Non-pathogenic mutations	Low probability variants	New pathogenic deletions	Known variants	Total
Number of subjects		61 (100%)	13 (100%)	3 (100%)	13 (100%)	90 (100%)
No consanguinity		57 (93%)	12 (92%)	3 (100%)	11 (85%)	84 (93%)
Age at onset	≤1 y.o.	54 (89%)	10 (77%)	3 (100%)	9 (69%)	76 (84%)
Status	Alive	33 (54%)	7 (54%)	1 (33%)	11 (85%)	53 (59%)
	Dead	28 (46%)	6 (46%)	2 (67%)	2 (15%)	37 (41%)
Sex	Female	30 (49%)	3 (23%)	2 (67%)	6 (46%)	41 (46%)
	Male	31 (51%)	10 (77%)	1 (33%)	7 (54%)	49 (54%)

y.o., years old.

Table 2. Summary of unreported mutations and deletions.

Patient ID	Age at onset	Clinical diagnosis	Enzyme assay (organ)	mtDNA variation	Locus	Heteroplasmy
377	1 year	LD	1 (Fb)	m.14439G>A	*ND6*	Homo (Fb)
190	1 year 6 months	LD	1,4 (M)	m.11246G>A	*ND4*	73% (fb)
508	0 days	SIDS	1 (Hep,Car)	m.4638A>G	*ND2*	86% (Fb), 0% (Hep, Car)
004	0 months	MC	1 (Fb)	m.5537A>G[1]	*tRNATrp*	27.4% (Fb)
271	0 months	ELBW	1 (Hep)	m.10045T>C	*tRNAGly*	Homo (hep)
312[2]	5 years	LD	1 (Fb) probably	m.1356A>G	*12S rRNA*	66% (Fb)
372	2 days	LIMD	1 (Hep)	Deletion (3424 bp) nt12493-15916		65.7% (Fb), 89.9% (Hep)
336	11 months	HD	1 (Hep)	Deletion (6639 bp) nt7734-14372		9.2% (Fb), 92.6% (Hep)
390	0 days	MC	1,4 (M,Hep)	Deletion (5424 bp) nt8574-13997		44.9% (Fb), 86.4% (Hep)

LIMD, lethal infantile mitochondrial disorder; HD, hepatic disease; LD, Leigh's disease; MC, mitochondrial cytopathy; SIDS, sudden infant death syndrome; ELBW, extremely low birth weight infant; Fb, fibroblast; Hep, liver; Car, heart; M, muscle.
[1]Expected to be causative because of the other reported mutation on the same position.
[2]m.1356A>G was confirmed as non-pathogenic and nDNA mutation was identified in Pt312.

showed bilateral and symmetrical hyperintensity foci in the basal ganglia. She developed progressive motor regression and became bedridden. Pt312 is a 5-year-old boy born after 36 weeks' gestation following a normal pregnancy to non-consanguineous parents. His birth weight was 2154 g. He has a sister who is his fraternal twin. At 5 months of age, his parents noticed hypotonia and nystagmus. At 10 months of age, he had generalized epilepsy and blood lactate and his pyruvate levels were high. A brain MRI revealed symmetrical high T2 signals in the midbrain.

Whole mtDNA sequencing and detection of variants

Genomic DNA (gDNA) was extracted from skin fibroblasts (Data S1), blood, liver, and cardiac muscle using either phenol/chloroform- or column-based extraction. Whole mtDNA was first polymerase chain reaction (PCR)-amplified as two separate large amplicons (LA1 and LA2) avoiding the nonspecific amplifications from nDNA.[9] Second-round PCR was performed using 46 primer pairs (mitoSEQrTM; Applied Biosystems, Carlsbad, CA) and the LA1 and LA2 amplicon mixture from first-round PCR as a template. PCR conditions were as follows: first-round PCR was performed in a reaction mixture containing 0.2 mmol/L of each dNTP, 0.25 U of Takara Ex Taq (Takara Bio, Shiga, Japan), 1× Ex Taq Buffer, 0.3 μmol/L of each primer, and extracted gDNA in a total volume of 50 μL. Initial denaturation was performed at 94°C for 2 min, followed by 30 cycles of 94°C for 20 sec, 60°C for 20 sec, and 72°C for 5 min, with a final extension at 72°C for 11 min. Second-round PCR was performed in a reaction mixture as

above except with a 10,000-fold dilution of LA1 amplicon and a 100-fold dilution of LA2 amplicon (total volume of the PCR reaction, 10 μL). Initial denaturation was performed at 96°C for 5 min, followed by 30 cycles of 94°C for 30 sec, 60°C for 45 sec, and 72°C for 45 sec, with a final extension at 72°C for 10 min.

First- and second-round PCR products were separated by 1% and 2% agarose gels, respectively, then 10 μL of second-round PCR products were incubated with 1 μL of ExoSAP-IT reagent (GE Healthcare UK Ltd., Bucks, U.K.) at 37°C for 30 min to degrade remaining primers and nucleotides. The ExoSAP-IT reagent was then inactivated by incubating at 75°C for 15 min. PCR products were sequenced using a BigDye Terminator v3.1 cycle sequencing kit (Applied Biosystems) and an ABI3130xl Genetic Analyzer (Applied Biosystems). Sequence data were compared with the revised Cambridge sequence (GenBank Accession No. NC_012920.1) and sequences present in MITOMAP (http://mitomap.org/MITOMAP) and mtSNP (http://mtsnp.tmig.or.jp/mtsnp/index_e.shtml) using SeqScape software (Applied Biosystems). Whole mtDNA sequencing of seven samples was obtained using an Ion PGM™ sequencer (Life Technologies Corporation, Carlsbad, CA).

Characterization of mtDNA deletions

We searched for mtDNA deletions by focusing on the size of first-round PCR products in agarose electrophoresis. If PCR products were smaller than controls, we suspected mtDNA deletion and performed further analysis. The smaller PCR products were recovered from the gel and amplified by second-round PCR, as described above, and
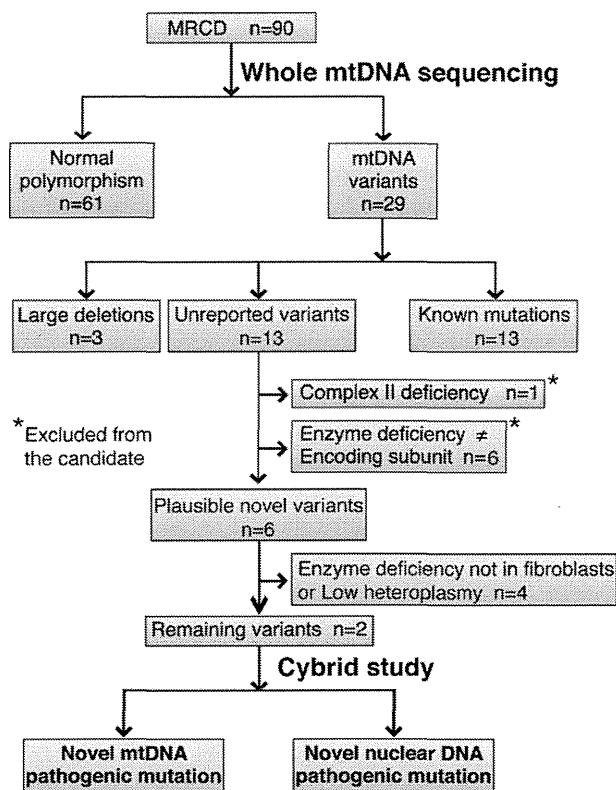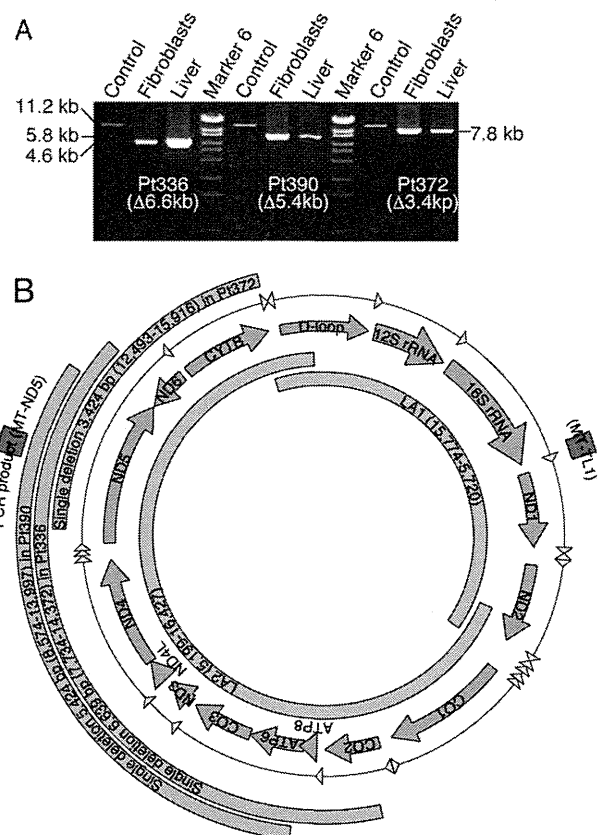
Figure 1. Flow diagram of study analysis. Ninety MRCD patients were analyzed in this study. Sixty-one patients had normal polymorphisms and 29 had mtDNA variants. Of these variants, 13 patients had MRCD causative mutations that had been previously described. We identified three novel large deletions and 13 unreported variants. Of the unreported variants, one patient with complex II deficiency was excluded because complex II is not encoded by mtDNA. Six patients were excluded because their enzyme deficiency pattern did not coincide with the variants found in mtDNA. Four patients were excluded because of the lack of fibroblast enzyme deficiency or low heteroplasmy. The remaining two cases were analyzed by cybrid study.

Figure 2. Identification of three large deletions. (A) Characterization of the three novel mtDNA deletions using agarose electrophoresis. First-round PCR products amplified from patient fibroblast and liver DNA clearly showed the presence of mtDNA deletions in Pt336, 390, and 372. Normal mtDNA from an MRCD patient was used as a positive control. (B) Positions of the novel mtDNA deletions are shown in blue. LA1 and LA2 amplification is shown in green. Two red squares represent real-time PCR amplicons MT-ND5 and MT-TL1.

analyzed for an mtDNA deletion. Second-round PCR was performed using fewer (25–26) PCR cycles to avoid untargeted DNA amplification. To identify the location of the deletion, we first compared the density of bands and screened the faint bands with agarose electrophoresis. The precise deletion boundaries were confirmed by sequencing analysis with primers used for second-round PCR that were close to the probable deletion region.

Results

Patient characteristics and their mtDNA mutations

A total of 90 patients (49 were men and 41 were women) with MRCD were subjected to whole mtDNA sequencing

analysis (Table 1). Eighty-four subjects (93%) were non-consanguineous. Seventy-six subjects (84%) were aged 1 year or younger. We identified 13 previously reported mtDNA mutations, 13 unreported variants, and three novel deletions (Fig. 1). The remaining 61 subjects had normal polymorphisms in their mtDNA (Fig. 1).

Large mtDNA deletions were identified in three patients

Agarose gel electrophoresis of first-round PCR from fibroblast and liver mtDNA clearly showed the presence of mtDNA deletions in Pt336, 390, and 372 (Fig. 2A). The precise deletion sites were confirmed by sequencing analysis. The expected size of the first-round PCR LA2 product in wild-type mtDNA from an MRCD patient was 11.2 kb, which enabled us to estimate the deletion sizes

of Pt336, 390, and 372 as 6639, 5424, and 3424 bp, respectively (Fig. 2A and B). In Pt336, the 6639-bp deletion was located between nucleotides 7734 and 14,372 and was flanked by 5-bp perfect direct repeats. This deletion results in the loss of 15 genes (*CO2, ATP8, ATP6, CO3, ND3, ND4L, ND4, ND5, ND6,* and six *tRNA* genes). The heteroplasmy ratio of this deletion was 9.2% in the fibroblasts (Fb) and 92.6% in the liver (Hep) (Table 2 and Data S1). In Pt390, the 5424-bp deletion was located between nucleotide positions 8574 and 13,997 and was flanked by 11-bp imperfect direct repeats. This deletion results in the loss of 11 genes (*ATP6, CO3, ND3, ND4L, ND4, ND5,* and five *tRNA* genes). The heteroplasmy ratio of this deletion was 44.9% (Fb) and 86.4% (Hep) (Table 2). In Pt372, the 3424-bp deletion was located between nucleotides 12,493 and 15,916 and was flanked by 6-bp imperfect direct repeats. This deletion results in the loss of five genes (*ND5, ND6, CYB,* and two *tRNA* genes). The heteroplasmy ratio of this deletion was 65.7% (Fb), and 89.9% (Hep) (Table 2).

Unreported variants of mtDNA detected in 13 patients

We identified 13 unreported mtDNA variants. Of these, seven were excluded by manual curation (Fig. 1). One of these was excluded because the enzyme deficiency was specific to complex II, which is not encoded by mtDNA. The other six were excluded because their enzyme deficiency pattern did not coincide with the variants found in mtDNA. From the remaining six plausible mtDNA variants, we determined whether they were causative using the following inclusion criteria for further analysis: (1) cells were viable for further assay, (2) mtDNA variants corresponded to the enzyme assay data in the RC subunit, (3) enzyme deficiency was observed in the fibroblasts, and (4) variants had high heteroplasmy ratios (Fig. 1 and Table 2). On the basis of these criteria, we selected two patients whose mtDNA variants (m.14439G>A in *MT-ND6* and m.1356A>G in *12S rRNA*) were suitable for further analysis as shown in Figure 1. The other four patients were excluded because they did not show enzyme deficiency in their fibroblasts or because of low heteroplasmy ratios (Table 2).

## m.14439G>A (*MT-ND6*), but not m.1356A>G (12S rRNA), is a causative mutation

The m.14439G>A (*MT-ND6*) variant was observed in fibroblasts from Pt377 (Fig. 3A). PCR- restriction fragment length polymorphism (RFLP) analysis with the *Hpy*188I restriction enzyme found Pt377 fibroblasts to be homoplasmic, and the m.14439G>A variant was not detected in

the blood of the patient's parents (Fig. 3A and B). This mutation changes the proline to a serine at amino acid position 79, which is highly conserved among vertebrates (Fig. 3C). ND6 is one of the mtDNA-encoded complex I subunits and alignment of the ND6 protein in different species revealed conservation of amino acids. The activity level of the RC complex I was coincidentally reduced in the patient's fibroblasts (Fig. 4A). To further confirm whether this mutation was causative of mitochondrial dysfunction, we performed cybrid analysis (Data S1). The cybrids showed a reduction in the complex I activity level consistent with the respiratory enzyme assay in the patient's fibroblasts (Fig. 4B). These data strongly support the idea that the m.14439G>A (*ND6*) mutation detected in Pt377 is responsible for the complex I deficiency.

The m.1356A>G (*12S rRNA*) variant was observed in fibroblasts from Pt312, which showed reduced activity levels of RC complex I (Fig. 4A). By mismatch PCR-RFLP-analysis using the *Sty*I restriction enzyme, this variant was determined at a heteroplasmy ratio of 66% in the patient's fibroblasts (Table 2). The cybrids harboring this variant showed a recovery of complex I enzyme activity compared with the original patient's fibroblasts (Fig. 4B). These data suggest that reduced complex I enzyme activity was rescued by nuclear DNA and that this mtDNA variation is not causative. This further indicates that the nuclear gene mutation is the cause of MRCD in this patient.

Identification of the c.55C>T (*NDUFA1*) mutation in Pt312 by whole exome sequencing

To search for the causative nuclear gene mutation in Pt312, we performed whole exome sequencing (Data S1). This identified a single hemizygous mutation (c.55C>T) in exon 1 of the *NDUFA1* gene, which altered the amino acid residue at position 19 from proline to serine (p. P19S). The mutation was confirmed by Sanger sequencing (Fig. 5A). This conserved proline residue lies within the hydrophobic N-terminal side constituting a functional domain that is involved in mitochondrial targeting, import, and orientation of *NDUFA1*.[10,11] SIFT and Poly-Phen, which predict the function of non-synonymous variants (http://genetics.bwh.harvard.edu/pph/), also revealed that the p.P19S mutation "probably" damages the function of the NDUFA1 protein (damaging score, 0.956). Alignment of the NDUFA1 protein between different species revealed the conservation of three amino acids, including the proline at position 19, which is highly conserved among vertebrates (Fig. 5B). To further confirm if the complex I deficiency in Pt312 occurred because of the mutation in *NDUFA1*, we overexpressed *NDUFA1* cDNA to determine if the enzyme deficiency
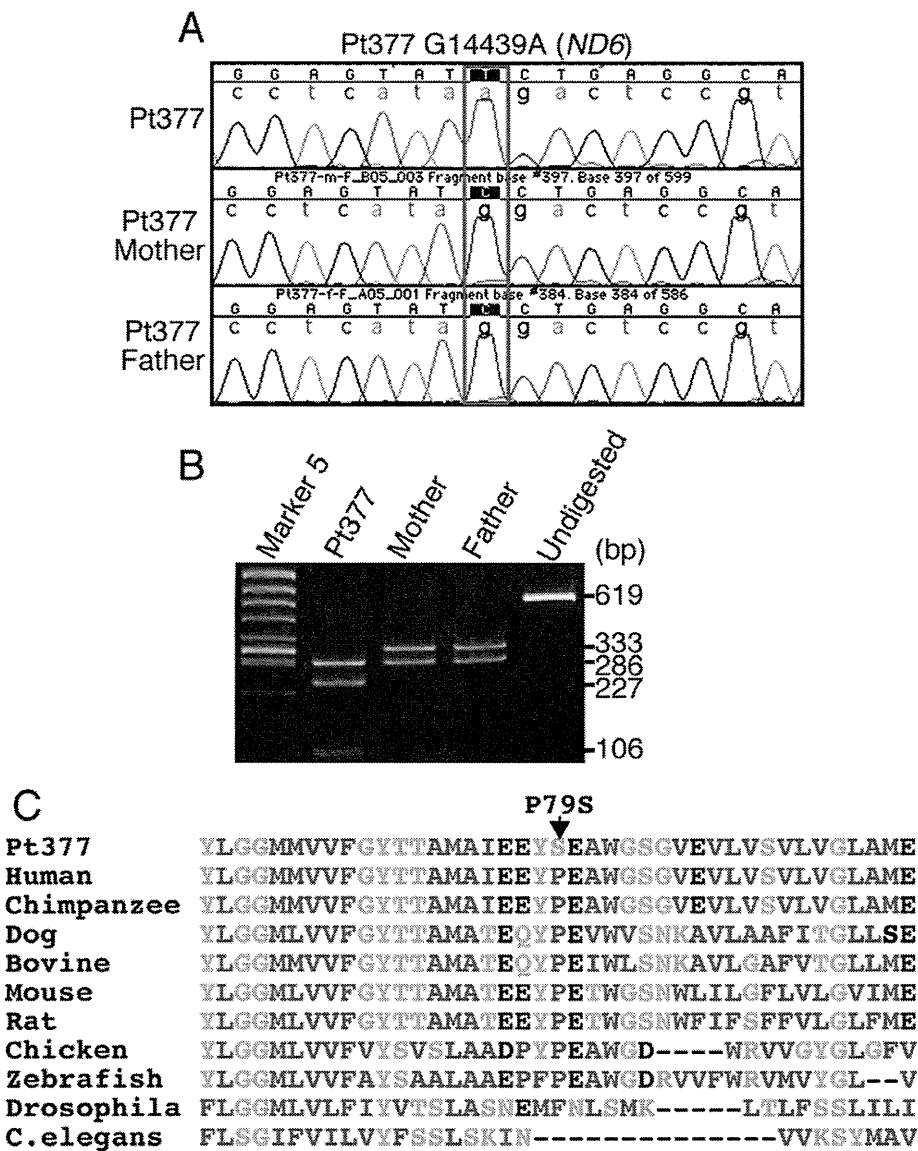
Figure 3. Novel mutation m.14439G>A in Pt377 mtDNA. (A) Trio-sequencing analysis of m.14439G>A (*MT-ND6* p.P79S) change in Pt377 family. Sequence chromatograms show that the m.14439G>A is detectable only in Pt377. (B) PCR-RFLPanalysis using fibroblast mtDNA from Pt377 and blood from both parents. A 619-bp PCR fragment was digested with *Hpy*188I. Wild-type mtDNA was cleaved into two fragments of 333 and 286 bp as shown in "Mother" and "Father", whereas the PCR product containing the m.14439G>A mutation was cleaved into three fragments: 286, 227, and 106 bp ("Pt377"). Undigested = undigested PCR product. (C) Alignment of MT-ND6 protein between different species shows the conservation of amino acid Proline 79. Amino acid sequences of *MT-ND6* gene products were aligned by ClustalW program (http://www.ebi.ac. uk/Tools/msa/clustalw2/) and NCBI/homologene (http://www.ncbi.nlm.nih.gov/homologene).

could be recovered (Data S1). Lentiviral transfection of NDUFA1 resulted in a significant increase in complex I assembly level as determined by blue native polyacrylamide gel electrophoresis. By contrast, lentiviral transfection of control mtTurboRFP did not rescue the phenotype (Fig. 5C). These data indicate that the c.55C>T mutation in *NDUFA1* is responsible for the complex I deficiency in Pt312.

Discussion

MRCD is particularly difficult to diagnose in pediatric cases as the clinical features are highly variable. We, therefore, propose a systematic approach for diagnosing MRCD that starts with a biochemical enzyme assay and is followed by whole mtDNA sequencing. In this study, we performed whole mtDNA sequencing for 90 children with

A

B
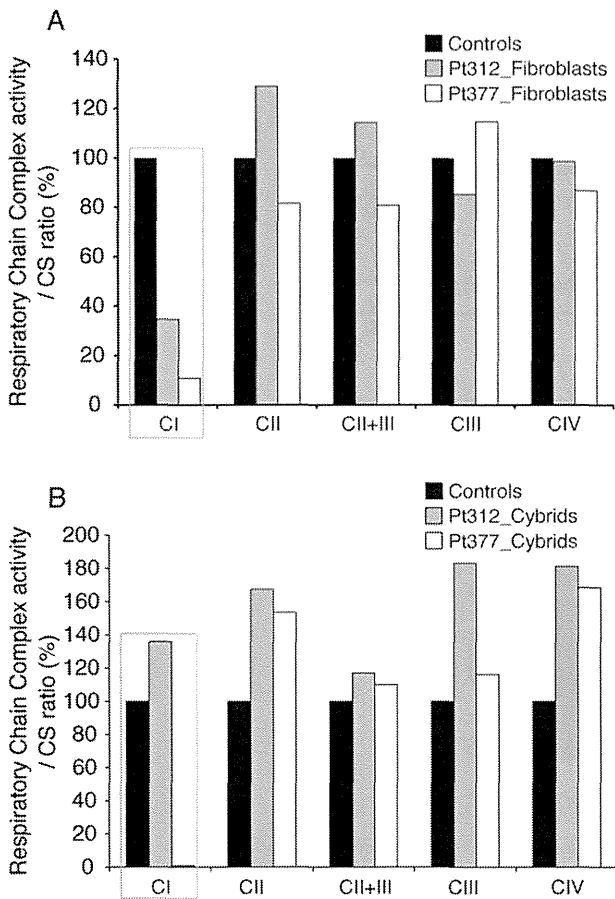
Figure 4. Biochemical assay for respiratory chain enzyme activity in fibroblasts and cybrid cells from Pt377 and Pt312. (A) Respiratory chain complex enzyme activity for CI, CII, CII + III, and CIV in skin fibroblast mitochondria from Pt312 and Pt377 compared with normal controls. The activity of each complex was calculated as a ratio relative to citrate synthase (CS). CI showed a reduction in enzyme activity in Pt312 and 377 fibroblasts. (B) Respiratory chain complex enzyme activity of cybrids established from Pt312 and Pt377 fibroblasts. Cybrids were established from rho0-HeLa cell and Pt312 or Pt377 fibroblasts. The activity of each complex in these cybrids was calculated as a ratio relative to that of citrate synthase (CS).

MRCD, and identified 29 mtDNA variants. Of these, we identified 13 known causative mutations, three large deletions, and further confirmed that m.14439G>A (*MT-ND6*) and c.55C>T (*NDUFA1*) are new causative mutations for MRCD from the results of a cybrid assay, whole exome sequencing, and a complementation study. The diagnosis of MRCD was then confirmed as definite by molecular analysis in these 18 cases.

Whole mitochondrial DNA sequencing identified 13 cases (14%) harboring known causative mtDNA mutations. mt. 10191T>C (*ND3*) and mt. 8993T>C or G (*ATP6*) mutations were detected in three and two patients, respectively (data not shown). Both are common causative muta-

tions of infantile Leigh syndrome. Previous reports found that most common MRCD causative mutations are primarily responsible for adult-onset disease, whereas few are responsible for childhood-onset MRCD;[12,13] only 14% of our cases were attributed to known mtDNA mutations.

Most patients in this study were 1-year old or younger at the onset of disease, with no family history. We used the RC complex enzyme assay to diagnose pediatric patients who had not been diagnosed with MRCD in a clinical setting. Several MRCD cases in children were previously reported to be difficult to diagnose with nonspecific clinical presentations in contrast to the characteristic clinical syndromes such as MELAS and MERRF caused by common mtDNA mutations.[6,12]

We identified three novel deletions that we concluded were causative because they include several genes that could explain the deficiency of the RC enzymes. Generally, most mtDNA deletions share similar structural characteristics, are located in the major arc between two proposed origins of replication (OH and OL; Mitomap), and are predominantly (~85%) flanked by short direct repeats.[14,15] Single mtDNA deletions are reported to be the common causes of sporadic MRCD such as Kearns-Sayre syndrome (KSS), CPEO, and Pearson's syndrome. In this study, all three deletions were located in the major arc and were flanked by repeat sequences, similar to previous studies. Although Pt390 was diagnosed with Pearson's syndrome, the other two patients (Pt336 and Pt372) did not show a common phenotype caused by a single deletion such as KSS, CPEO, or Pearson's syndrome. Therefore, screening by mtDNA size differences is important even in those patients not clinically suspected to have mtDNA deletions.

Manual curation identified six plausible mtDNA variants that had not previously been reported (Fig. 1). We attempted to carry out a functional assay of the two patients whose fibroblasts are enzyme deficient, although it was difficult to apply this strategy to those fibroblasts with normal enzyme activity. In this sense, it is important to collect patients with similar phenotypes and carrying the same mtDNA variants to accurately diagnose the causal mutation. Thus, this study of patients harboring unreported mtDNA variants will be useful in a clinical situation. Of these, the m.14439G>A (*MT-ND6*) variant was experimentally confirmed to be a novel causative mtDNA mutation, while 1356A>G (*12S rRNA*) was confirmed to be non-pathogenic by a cybrid assay. The remaining four novel variants have yet to be experimentally elucidated, but m.5537A>G (*mt-tRNA trp*) in Pt004 is likely to be causative because m.5537AinsT was reported to be disease causing.[16]

ND6 is an mtDNA-encoded complex I subunit that is essential for the assembly of complex I and the maintenance of its structure.[17-19] *ND6* mutations were previ-